CDDpress

www.nature.com/cdd

ARTICLE

Ferroptotic stress facilitates smooth muscle cell dedifferentiation in arterial remodelling by disrupting mitochondrial homeostasis

Qing-Xin Ji[1,2,7], Fei-Yan Zeng[3,7], Jian Zhou[4,7], Wen-Bin Wu[1,7], Xu-Jie Wang[1,2], Zhen Zhang[1,2], Guo-Yan Zhang[1,2], Jie Tong[1,2], Di-Yang Sun[1], Jia-Bao Zhang[1], Wen-Xiang Cao[1], Fu-Ming Shen[2], Jin-Jian Lu[5], Dong-Jie Li[2,6,8]✉ and Pei Wang[1,8]✉

© The Author(s), under exclusive licence to ADMC Associazione Differenziamento e Morte Cellulare 2022

Smooth muscle cell (SMC) phenotypic switch from a quiescent 'contractile' phenotype to a dedifferentiated and proliferative state underlies the development of cardiovascular diseases (CVDs); however, our understanding of the mechanism is still incomplete. In the present study, we explored the potential role of ferroptosis, a novel nonapoptotic form of cell death, in SMC phenotypic switch and related neointimal formation. We found that ferroptotic stress was triggered in cultured dedifferentiated SMCs and arterial neointimal tissue of wire-injured mice. Moreover, pro-ferroptosis stress was activated in arterial neointimal tissue of clinical patients who underwent carotid endarterectomy. Blockade of ferroptotic stress via administration of a pharmacological inhibitor or by global genetic overexpression of glutathione peroxidase-4 (GPX4), a well-established anti-ferroptosis molecule, delayed SMC phenotype switch and arterial remodelling. Conditional SMC-specific gene delivery of GPX4 using adreno-associated virus in the carotid artery inhibited ferroptosis and prevented neointimal formation. Conversely, ferroptosis stress directly triggered dedifferentiation of SMCs. Transcriptomics analysis demonstrated that inhibition of ferroptotic stress mainly targets the mitochondrial respiratory chain and oxidative phosphorylation. Mechanistically, ferroptosis inhibition corrected the disrupted mitochondrial homeostasis in dedifferentiated SMCs, including enhanced mitochondrial ROS production, dysregulated mitochondrial dynamics, and mitochondrial hyperpolarization, and ultimately inhibited SMC phenotypic switch and growth. Copper-diacetyl-bis^{N4}-methylthiosemicarbazone (CuATSM), an agent used for clinical molecular imaging and that potently inhibits ferroptosis, prevented SMC phenotypic switch, neointimal formation and arterial inflammation in mice. These results indicate that pro-ferroptosis stress is likely to promote SMC phenotypic switch during neointimal formation and imply that inhibition of ferroptotic stress may be a promising translational approach to treat CVDs with SMC phenotype switch.

Cell Death & Differentiation (2023) 30:457–474; https://doi.org/10.1038/s41418-022-01099-5

INTRODUCTION

Unlike skeletal muscle and cardiac muscle, which mainly consist of terminally differentiated cells, smooth muscle cells (SMCs) in arterial vessels retain remarkable plasticity and can undergo a phenotypic switch in response to environmental and internal cues from the contractile phenotype to a dedifferentiated phenotype, including proliferation, migration, proinflammation and extracellular matrix molecule secretion. Unravelling the mechanisms involved in the fate and state of SMCs is an important step towards a better understanding of the pathology of cardiovascular diseases (CVDs) [1–3]. Currently, ample evidence has suggested that biomechanical stimulating factors such as blood shear stress and stretch drive the phenotypic switch of SMCs. In contrast, the involvement of cell death in SMC dedifferentiation in phenotypic switch is less well understood. Modulating cell death such as apoptosis is considered to be a potential therapeutic option for CVDs associated with SMC phenotypic switch [4–6].

Ferroptosis was originally defined in 2012 as a novel form of regulated cell death (RCD) characterized by ferrous iron (Fe^{2+})-dependent lethal lipid hydroperoxide accumulation [7]. Ferroptosis is morphologically, biochemically, and genetically distinct from other well-known cell death types such as apoptosis and necroptosis. The main molecular mechanisms of ferroptosis involve the biological toxicity of Fe^{2+}-produced highly active reactive oxygen species (ROS), which in turn attack biomembranes [7–9]. Damaged and oxidated phospholipids containing polyunsaturated fatty acids (PUFAs) in biomembranes initiate ferroptotic cell death [7–9]. Dysfunction of glutathione

[1]Department of Pharmacology, School of Pharmacy, Naval Medical University/Second Military Medical University, Shanghai, China. [2]Department of Pharmacy, Shanghai Tenth People's Hospital, Tongji University School of Medicine, Shanghai, China. [3]Department of Pharmacology, Shanghai Forth People's Hospital, Tongji University School of Medicine, Shanghai, China. [4]Department of Cardiac Surgery, Shanghai Tenth People's Hospital, Tongji University School of Medicine, Shanghai, China. [5]State Key Laboratory of Quality Research in Chinese Medicine, Institute of Chinese Medical Sciences, University of Macau, Macao, China. [6]Institute of Nuclear Medicine, Tongji University School of Medicine, Shanghai, China. [7]These authors contributed equally: Qing-Xin Ji, Fei-Yan Zeng, Jian Zhou, Wen-Bin Wu. [8]These authors jointly supervised this work: Dong-Jie Li, Pei Wang. ✉email: djli@tongji.edu.cn; pwang@smmu.edu.cn

Edited by D. Aberdam

Received: 26 July 2022 Revised: 22 November 2022 Accepted: 24 November 2022
Published online: 7 December 2022

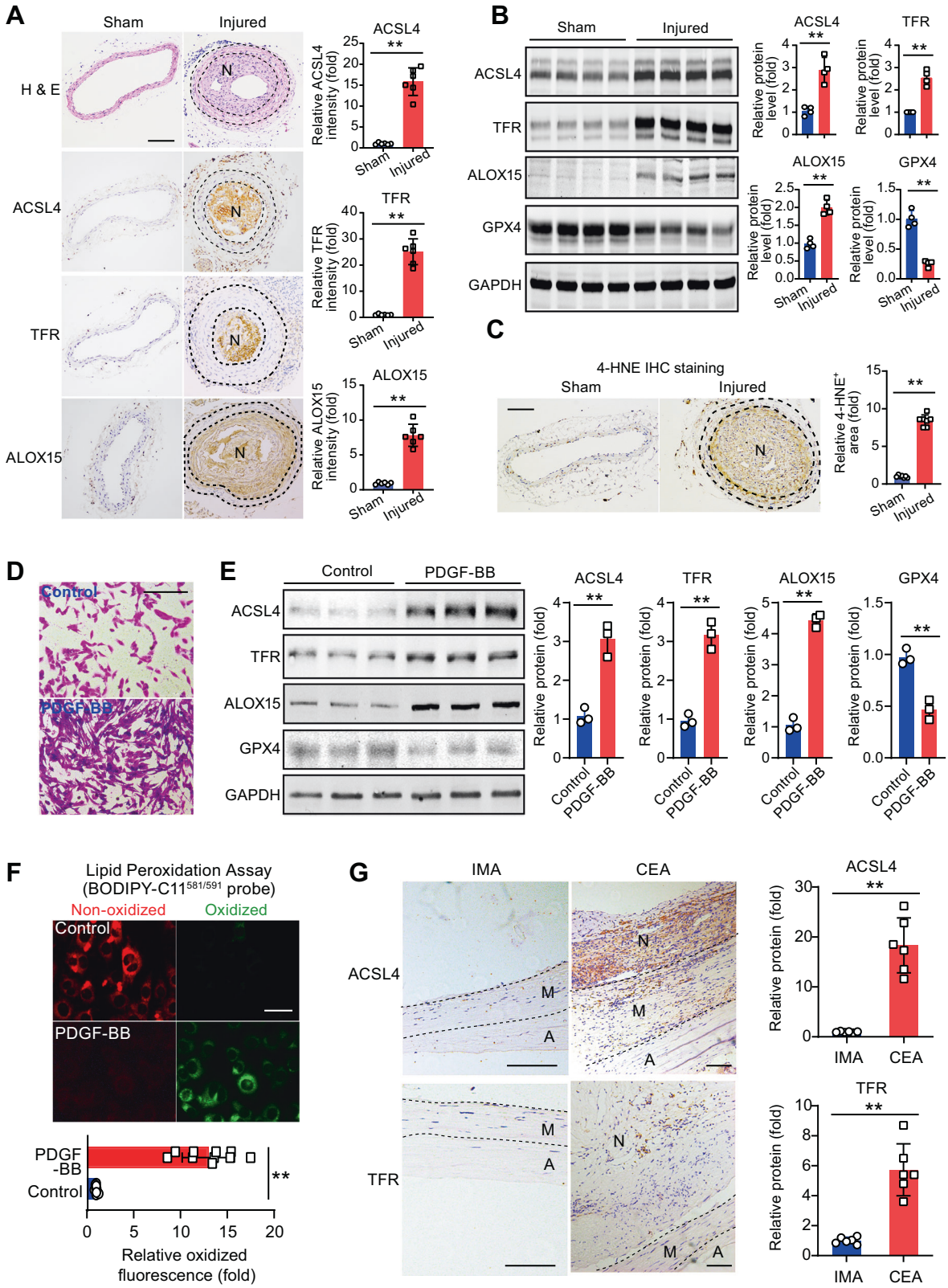

peroxidase 4 (GPX4) and subsequent deficits in the lipid-oxidation preventive system are major regulatory mechanisms of ferroptosis [8, 9]. In addition to GPX4, ferroptosis is also regulated by the coenzyme-Q system (ferroptosis suppressor protein 1 [FSP1] [10–12] and dihydroorotate dehydrogenase [DHODH] [13], energy production masters [14–16], long non-coding RNAs [17], ubiquitin system [18, 19], tumour-related genes [20, 21], selenium [22], calcium [23], etc. In the cardiovascular system, ferroptosis has been reported to be associated with cell death in cardiomyopathy [24, 25] and

Fig. 1 Ferroptotic stress correlates with the dedifferentiation of SMCs. A Representative histological and immunohistochemical images and quantitative analyses of pro-ferroptotic markers ACSL4, TFR and ALOX15 in carotid arteries from mice with sham-operation (Sham) and wire-injure (Injured). These factors were detected mainly in neointimal tissue but not arterial media layer. Scale bar, 100 μm. $n = 6$ biological replicates per group. ACSL4, acyl-CoA synthetase long-chain family member 4; ALOX15, arachidonate 15-lipoxygenase; TFR, transferrin receptor. **B** Representative immunoblotting and quantitative analyses of pro-ferroptotic molecules (ACSL4, TFR and ALOX15) and anti-ferroptotic molecule GPX4 in carotid arteries from two groups of mice. n = 4 biological replicates per group. GPX4, glutathione peroxidase 4. **C** Representative immunohistochemical images and quantitative analyses of lipid peroxidation marker 4-HNE in arteries from mice with sham-operation (Sham) and wire-injure (Injured). Scale bar, 100 μm. $n = 6$ biological replicates per group. **D** Crystal violet staining of dedifferentiated SMCs induced by PDGF-BB treatment (20 ng/ml). Scale bar, 20 μm. **E** Representative immunoblotting images and quantitative analyses of pro-ferroptotic molecules (ACSL4, TFR and ALOX15) and anti-ferroptosis molecule GPX4 in primary human aortic SMCs in response to PDGF-BB treatment. $n = 3$ biological replicates per group. **F** Evaluation of lipid peroxidation in dedifferentiated SMCs using BODIPY-C11$^{581/591}$ probe. The non-oxidized (red) and oxidized (green) forms of BODIPY-C11$^{581/591}$ probe were detected in two channels. The green signal was calculated for lipid peroxidation level. Scale bar, 10 μm. $n = 10$ biological replicates per group. **G** Representative immunohistochemical images of pro-ferroptotic molecules ACSL4 and TFR in arterial neointimal tissues of patients who underwent carotid endarterectomy (CEA) compared with control normal internal mammary artery (IMA) used for coronary artery bypass graft surgery. Scale bar, 100 μm. $n = 6$ biological replicates per group. N, neointimal tissue; M, media; A, adventitia. Data expressed as mean ± SEM. Comparisons of parameters were performed with unpaired two-sided Student *t* test. $^{**}P < 0.01$.

endothelial cells [26]. However, the role of ferroptosis in SMC phenotype maintenance and switching is largely unknown.

In the present study, we demonstrate that pro-ferroptosis stress is activated in dedifferentiated SMCs in vitro and in vivo in both a mouse model and patients. Unexpectedly, instead of inducing SMC death, the ferroptotic stress promotes SMC phenotypic switch by sustaining their dedifferentiation.

RESULTS

Activated ferroptotic stress correlates with the dedifferentiation of SMCs in vitro and in vivo

To understand the alteration of ferroptotic signalling (Fig. S1) in SMC dedifferentiation, we examined several ferroptosis-related factors in a neointimal hyperplasia mouse model with SMC dedifferentiation followed by carotid artery injury, including acyl-CoA synthetase long-chain family member 4 (ACSL4) [27, 28], transferrin receptor (TFR) [29], and arachidonate 15-lipoxygenase (ALOX15) [30]. These pro-ferroptotic molecules were induced in the neointimal tissue (Fig. 1A). Immunoblotting confirmed the changes in these three pro-ferroptotic molecules and further showed that GPX4, a dictator of the anti-ferroptosis system [8], declined in the injured arteries (Fig. 1B). In addition, immunohistochemistry of 4-hydroxynonenal (4-HNE), a marker of lipid peroxidation, was remarkably triggered (Fig. 1C). However, using TUNEL staining, we found no obvious cell death in the neointimal tissues from model mice (Fig. S2A) and patients who underwent carotid endarterectomy (CEA) (Fig. S2B). In the single-cell suspensions extracted from arteries of both sham-operated and injured mice, we did not observe cells positive for 7-AAD, a specific probe of cell death (Fig. S2C). These results suggest a shift towards a pro-ferroptotic state in dedifferentiated SMCs in neointimal tissue, although there is no real ferroptosis in the neointima.

Next, we sought to confirm this observation by determining whether pro-ferroptotic signalling was activated by platelet-derived growth factor BB (PDGF-BB), a growth factor that promotes SMC dedifferentiation in an in vitro model. In cultured primary human aortic SMCs PDGF-BB induced pronounced SMC proliferation (Fig. 1D) and activated pro-ferroptosis signalling (Fig. 1E). The ferroptotic stress within the dedifferentiated SMCs was further assessed by the BODIPY-C11$^{581/591}$ probe (Fig. 1F). We observed that the pro-ferroptotic markers ACSL4 and TFR were increased in arterial neointimal tissues from patients with CEA compared with control internal mammary arteries (IMAs) used for coronary artery bypass graft surgery (Fig. 1G). There were no significant differences in clinical characteristics between the patients (Table. SI). Together, these findings indicate that activated ferroptotic stress correlates with SMC dedifferentiation.

Ferroptosis inhibitor restrains phenotype switch in dedifferentiated SMCs

To ascertain the essential role of the activation of pro-ferroptotic signalling in SMC phenotype switch, we studied cultured human aortic SMCs treated with the ferroptosis inhibitor ferrostatin-1 (Fer-1, Fig. S3A) [7]. Flow cytometry and immunofluorescent assays with the BODIPY-C11$^{581/591}$ probe showed that Fer-1 blocked lipid peroxidation in dedifferentiated SMCs (Fig. S3B-C). In accordance, the reduced level of glutathione, a cofactor of GPX4, as well as the enhanced level of malondialdehyde (MDA), a product of oxidative PUFAs, were reversed by Fer-1 in dedifferentiated SMCs (Fig. S3D). Fer-1 also significantly downregulated ACSL4 protein expression (Fig. S3E). These results confirmed the potent inhibitory effect of Fer-1 on ferroptotic signalling in cultured dedifferentiated SMCs.

Next, we evaluated the influence of Fer-1 on SMC phenotype switch. The CCK-8 assay showed that Fer-1 treatment significantly impeded the enhanced cell proliferation induced by PDGF-BB (Fig. 2A). Immunofluorescent 5-ethynyl-2′-deoxyuridine (EdU) incorporation assays confirmed the inhibitory action of Fer-1 on SMC proliferation (Fig. 2B). Two proliferative markers, PCNA (encoded by *Pnca*) and Cyclin D1 (encoded by *Ccnd1*), were induced at both the mRNA and protein levels in dedifferentiated SMCs and were repressed by Fer-1 (Fig. 2C, D). *Mmp2* and *Mmp9*, two genes important in SMC migration, were induced in dedifferentiated SMCs but inhibited by Fer-1 (Fig. 2E). Accordingly, transwell and wound healing assays demonstrated that the enhanced SMC migration was inhibited by Fer-1 (Fig. 2F, G). Osteopontin (OPN) and vimentin, two markers of the synthetic phenotype of SMCs, were upregulated in dedifferentiated SMCs but blocked by Fer-1 (Fig. 2H). Conversely, the mRNA levels of the SMC contractile markers *Cnn1* and *SM22α* were significantly lowered in dedifferentiated SMCs and rescued by Fer-1 (Fig. 2I). In parallel, the decreases in Calponin-1 (encoded by *Cnn1*) and transgelin (encoded by *Cnn1*) protein were prevented by Fer-1 treatment (Fig. 2J). Together, these results suggest that blockade of ferroptotic signalling by a selective inhibitor restrains SMC phenotypic switch.

Overexpression of GPX4 restrains SMC phenotype switch and dedifferentiation

To exclude the potential off-target action of pharmacological inhibitors, we used a genetic approach to overexpress GPX4 in SMCs (Fig. 3A). GPX4 overexpression significantly counteracted the shift of the BODIPY-C11 probe from the nonoxidized form to the oxidized form (Fig. 3B) and reduced the levels of MDA and 4-HNE (Fig. 3C). The increased levels of ferroptotic markers in dedifferentiated SMCs were partially inhibited by GPX4 overexpression (Fig. 3D). EdU assays showed that GPX4 overexpression displayed potent inhibition of SMC proliferation (Fig. 3E). The SMC

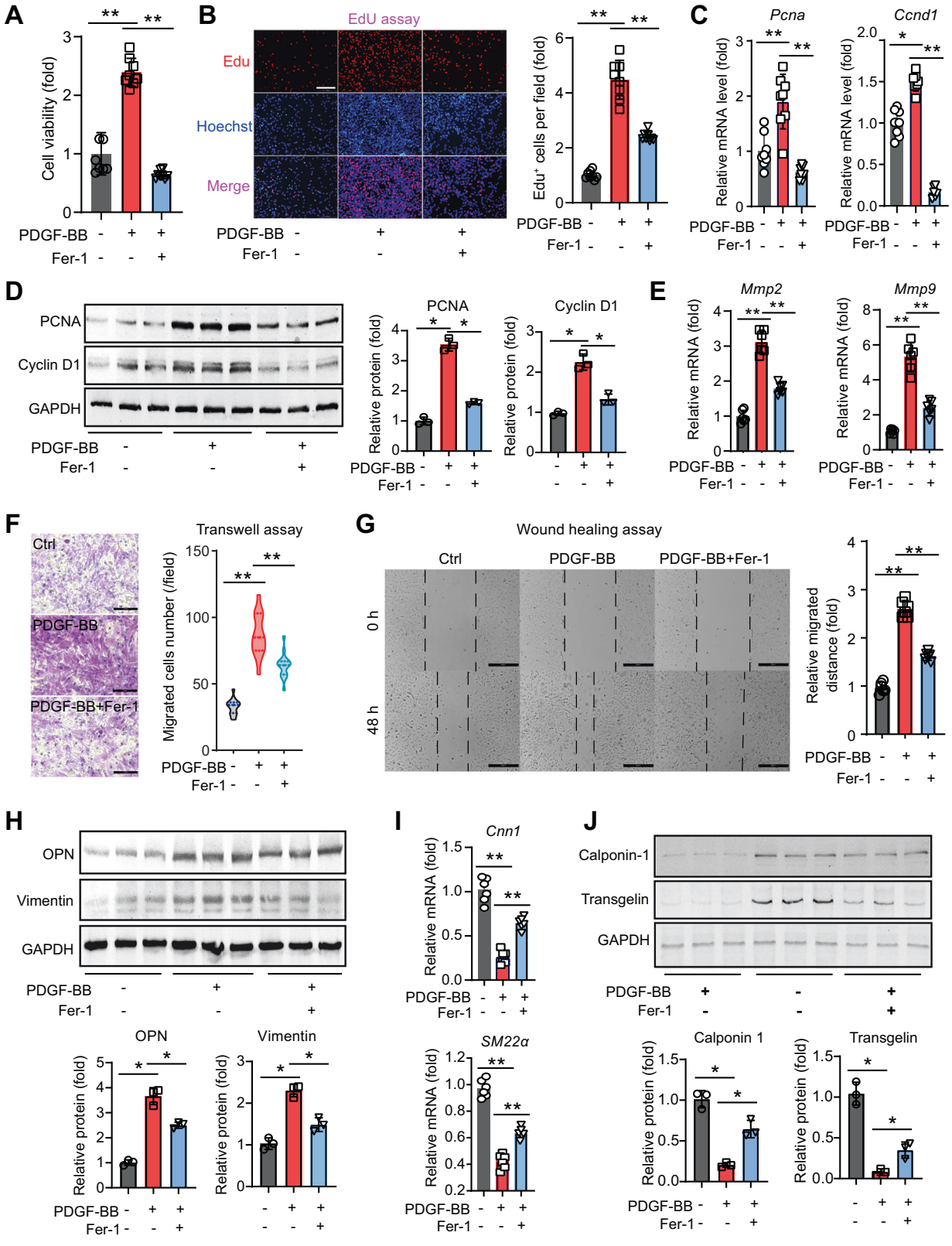

proliferative markers PCNA and Cyclin D1 were induced in dedifferentiated SMCs but suppressed by GPX4 overexpression (Fig. 3F). SMC migration was also hindered by GPX4 overexpression, as evidenced by the results of transwell and wound healing assays (Fig. 3G). Immunoblotting of the SMC migration markers MMP2 and MMP9 confirmed the inhibitory effect of GPX4 overexpression on SMC migration (Fig. 3H). The protein levels of the SMC synthetic markers OPN and vimentin were also increased in dedifferentiated SMCs but were suppressed by GPX4 overexpression (Fig. 3I). In accordance, the decreased mRNA levels of

Fig. 2 Ferroptosis inhibitor ferrostatin-1 (Fer-1) suppresses phenotype switch in dedifferentiated SMCs. A Cell proliferation analysis by CCK-8 assay in primary cultured human aortic SMCs treated by PDGF-BB (20 ng/ml) or PDGF-BB plus Fer-1 (2 μM). PDGF-BB was used to induce proliferation and growth. $n = 8$ biological replicates per group. **B** Proliferation analysis in dedifferentiated human aortic SMCs using fluorescent EdU assay. EdU dye was incorporated into proliferative cells (red). DAPI was used to stain nuclei (blue). $n = 8$ fields biological replicates per group. **C** Quantitative PCR analyses of proliferative genes *Pcna* and *Ccnd1* in SMCs treated by PDGF-BB or PDGF-BB + Fer-1. $n = 8$ biological replicates per group. **D** Immunoblotting analyses of PCNA (encoded by *Pcna*) and Cyclin D1 (encoded by *Ccnd1*) in SMCs treated by PDGF-BB or PDGF-BB + Fer-1. $n = 8$ biological replicates per group. **E** Quantitative PCR analyses of migration-related genes *Mmp2* and *Mmp9* in SMCs treated by PDGF-BB or PDGF-BB + Fer-1. $n = 8$ biological replicates per group. **F** Evaluation of SMC migration using transwell assay in SMCs treated by PDGF-BB or PDGF-BB + Fer-1. $n = 20$ biological replicates per group. **G** Evaluation of migration using wound healing assay (scratch assay) in SMCs treated by PDGF-BB or PDGF-BB + Fer-1. $n = 20$ biological replicates per group. The gap created by scratch at two time-points (0 h and 24 h) and the migration of SMCs was calculated. **H** Immunoblotting analyses of synthetic markers osteopontin (OPN) and vimentin in SMCs treated by PDGF-BB or PDGF-BB + Fer-1. $n = 3$ biological replicates biological per group. **I** Quantitative PCR analyses of SMC contractile-related genes *Cnn1* and *SM22α* in SMCs treated by PDGF-BB or PDGF-BB + Fer-1. n = 6 biological replicates per group. **J** Immunoblotting analyses of SMC contractile-related molecules Calponin-1 (encoded by *Cnn1*) and transgelin (encoded by *SM22α*) in SMCs treated by PDGF-BB or PDGF-BB + Fer-1. $n = 3$ biological replicates per group. Data expressed as mean ± SEM. Comparisons were performed with One-Way ANOVA unpaired Tukey-hoc test. $^{*}P < 0.05$, $^{**}P < 0.01$.

the SMC contractile markers *Cnn1*, *SM22α* and *Acta2* in dedifferentiated SMCs were reversed by GPX4 overexpression (Fig. 3J). These results further support that the enhanced ferroptotic stress facilitates SMC phenotype switch, which is restrained by GPX4-mediated anti-ferroptosis bioactivity.

Ferroptosis stress directly triggers dedifferentiation of SMCs without PDGF-BB

To further decipher the role of ferroptosis stress in SMCs, we next determined whether ferroptosis stress can directly trigger dedifferentiation of SMCs in the absence of PDGF-BB stimulation. The ferroptosis inducer RSL-3 was added to the culture medium of human aortic SMCs at a low concentration (5 ng/ml, without obvious cytotoxicity) for 48 h. We found that RSL-3 treatment significantly reduced the SMC contractile markers calponin-1 and transgelin and induced the SMC synthetic marker vimentin (Fig. S4A). We also used immunofluorescent staining of OPN to evaluate SMC dedifferentiation. The RSL-3-treated SMCs were flat and enlarged in morphology, and RSL-3 treatment induced OPN expression (Fig. S4B). These results suggested that ferroptosis stress directly triggers the dedifferentiation of SMCs without PDGF-BB.

Knockin of GPX4 delays SMC phenotype switch and arterial remodelling in mice

To evaluate the role of ferroptotic stress in SMC phenotypic switch in vivo, we used a mouse strain with genetic knock-in of CAG-promoter-driven GPX4 cDNA into the Rosa26 locus to increase GPX4 protein levels globally (Fig. S5A) [31]. Immunoblotting demonstrated the overexpression of GPX4 in the mouse carotid aorta (Fig. S5B). The overexpression of GPX4 in carotid aortae from GPX4-knockin mice was confirmed (Fig. S5C). There was no difference in body weight, blood pressure, or plasma lipids between the two groups before and after injury (Table. S2). Compared with the WT mice, the GPX4-KI mice had significantly inhibited ferroptotic stress in the neointimal tissue of injured arteries, as evidenced by the downregulated ACSL4 and TFR in immunoblotting (Fig. S5D), reduced iron accumulation in Prussian blue staining (Fig. S5E), depressed ALOX15 in immunohistochemistry (Fig. S5F), retained glutathione content (Fig. S5G) and suppressed MDA level (Fig. S5H). These results also confirmed the successful overexpression of GPX4 in GPX4-KI mice.

As expected, the postinjury neointimal area in the GPX4-KI mice was significantly thinner than that in WT mice (Fig. 4A). Accordingly, the levels of SMC proliferation markers (Cyclin D1 and PCNA) and synthetic markers (OPN and vimentin) in GPX4-KI injured arteries were lower than those in WT arteries after injury (Fig. 4B). Picrosirius staining under polarization microscopy demonstrated that type III collagen fibres (green), which were typically expressed by synthetic SMCs, were clearly observed in the core area of the neointima in WT mice (Fig. 4C, upper panel). In contrast, the neointima in GPX4-KI mice had more type I collagen fibres (orange) and fewer type III collagen fibres (Fig. 4C, lower panel). GPX4-KI mice also had smaller MMP2- and MMP9-positive neointimal areas than WT mice (Fig. 4D). In line with these findings, the mRNA expression levels of *Cnn1* and *SM22α* were remarkably downregulated in the neointima of WT mice and to a lesser extent in that of GPX4-KI mice (Fig. 4E). Finally, we found that proinflammatory factors, including interleukin-1β (IL-1 β), monocyte chemoattractant protein-1 (MCP-1) and C-X3-C-motif chemokine receptor 1 (CX3CR1), were abundantly expressed in the arterial neointima of WT mouse and, to a much lesser extent, in that of GPX4-KI mouse (Fig. 4F). These results indicate that global overexpression of GPX4 in mice protects against postinjury SMC phenotypic switch.

Conditional SMC-specific gene delivery of GPX4 retards SMC phenotype switch and arterial remodelling

We constructed an adeno-associated virus serotype-2/9 (AAV) encoding mouse GPX4 (Fig. 5A) under the control of an SMC-specific SM22α promoter (AAV2/9-SM22α-mGPX4-Flag-ZsGreen, referred to as AAV-vGPX4) and its control virus (AAV2/9-SM22α-ZsGreen, referred to as AAV-control) and administered them to injured mice (Fig. S6A). No obvious difference was observed in body weight or plasma lipids among the groups (Table. S5). Immunofluorescence showed SMC-specific expression of ZsGreen-labelled GPX4 (Fig. S6B). AAV-vGPX4 induced GPX4 mRNA (Fig. 5B) and protein expression (Fig. 5C) in carotid arteries. Treatment with AAV-vGPX4 significantly reduced the neointimal area in injured mice (Fig. 5D) and inhibited 4-HNE and MDA (Fig. 5E, F). Abundant expression of SMC proliferation markers and synthetic markers was observed in neointimal tissue but not arterial media (Fig. 5G, H). AAV-vGPX4 gene therapy reduced neointimal SMC proliferation markers (Fig. 5G) but decreased neointimal SMC synthetic phenotype markers (Fig. 5H). In accordance, the synthesized collagen contents in neointimal tissue were inhibited by AAV-vGPX4 therapy, as evidenced by the results from Masson's Trichrome staining and Picrosirius Red staining (Fig. 5I). Conversely, contractile markers were significantly preserved in carotid arteries from mice with AAV-vGPX4 administration (Fig. 5J). The levels of proinflammatory factors and chemokines were inhibited by AAV-vGPX4 therapy (Fig. 5K). These results indicate that conditional SMC-specific GPX4 gene delivery blocks SMC dedifferentiation and retards neointima formation in mice.

Inhibition of ferroptotic stress suppresses the mitochondrial respiratory chain in arterial remodelling

To further understand the molecular mechanism by which ferroptosis inhibition modulates the SMC phenotype, injured arteries from WT and GPX4-KI mice were subjected to RNA sequencing for comparison of differentially expressed genes

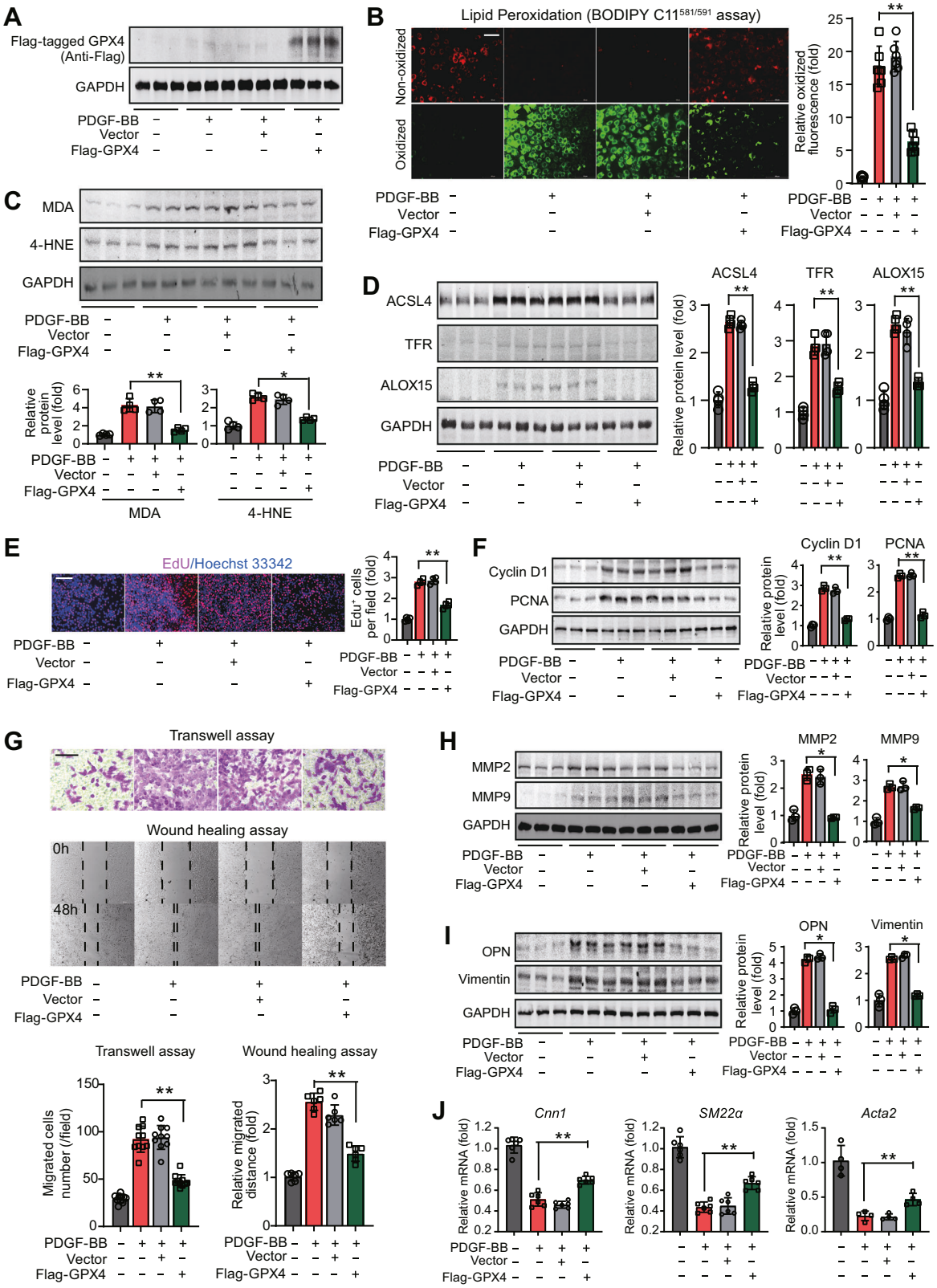

(DEGs, Fig. 6A and Fig. S7A–B). Correlation analysis between samples and principal component analysis (PCA) showed that the overall transcriptomes of arteries from WT and GPX4-KI mice were separated (Fig. 6B, C). The total heatmap of differentially expressed genes is illustrated in Fig. 6D. Compared with injured arteries from WT mice, the injured arteries from GPX4-KI mice had 169 upregulated and 324 downregulated DEGs (criteria: $P < 0.01$, fold change >2 or <0.5, Fig. 6E). The top 20 downregulated and upregulated DEGs are illustrated in Fig. 6F. It was noted that many downregulated DEGs in injured arteries of GPX4-KI mice were

Fig. 3 Overexpression of GPX4 restrains phenotype switch in dedifferentiated SMCs. A Immunoblotting analysis of the overexpressed GPX4 using an antibody against Flag-tag. The plasmid carrying Flag-tagged mouse GPX4 was overexpressed into mouse SMCs (MOVAS cells). The empty vector plasmid was also overexpressed as a vector control. PDGF-BB was administrated to induce SMC dedifferentiation. $n = 3$ biological replicates per group. **B** Evaluation of lipid peroxidation in dedifferentiated mouse SMCs with GPX4 overexpression using fluorescence of BODIPY-C11$^{581/591}$ probe in dedifferentiated SMCs. The green signal (oxidized form of BODIPY-C11$^{581/591}$ probe) was calculated for lipid peroxidation level. n = 6 biological replicates per group. Scale bar, 20 μm. **C** Two markers of lipid peroxidation malondialdehyde (MDA) and 4-hydroxynonenal (4-HNE) were determined in dedifferentiated mouse SMCs. $n = 3$ biological replicates per group. **D** Pro-ferroptotic molecules ACSL4, TFR and ALOX15 were determined in dedifferentiated mouse SMCs. $n = 3$ biological replicates per group. **E** Proliferation analysis in dedifferentiated mouse SMCs using fluorescent EdU assay (red). DAPI was used to stain nuclei (blue). $n = 6$ biological replicates per group. **F** Immunoblotting analyses of Cyclin D1 and PCNA in dedifferentiated mouse SMCs. n = 3 biological replicates per group. **G** Evaluation of SMC migration using transwell assay and wound healing assay (scratch assay) in dedifferentiated mouse SMCs. $n = 8$ biological replicates per group. The gap created by scratch at two time-points (0 h and 24 h) and the migration of SMCs was calculated. **H** Immunoblotting analyses of matrix metallopeptidase 2 (MMP2) and MMP9 in dedifferentiated mouse SMCs. $n = 3$ biological replicates biological per group. **I** Immunoblotting analyses of synthetic markers osteopontin (OPN) and vimentin in dedifferentiated mouse SMCs. $n = 3$ biological replicates biological per group. **J** Quantitative PCR analyses of SMC contractile-related genes *Cnn1*, *SM22α* and *Acta2* in dedifferentiated mouse SMCs. $n = 4$-6 biological replicates per group. Data expressed as mean ± SEM. GAPDH was used as a loading control in immunoblotting. Comparisons were performed with unpaired two-sided Student *t* test. The values of blank and empty vector-overexpressed groups were not included for comparison. $^{*}P < 0.05$, $^{**}P < 0.01$.

mitochondria-specific genes, including *mt-Nd1*, *mt-Nd2, mt-Nd3, mt-Nd4, mt-Nd6*, and *Ckmt2* (creatine GPX4-KInase 2, mitochondrial, Fig. 6F). Bioinformatical correlation analysis through the use of corrplot packages demonstrated the correlation among these top 40 DEGs and suggested that the abundance of genes *Id1*, *Ccdc24*, *Cntnap2*, *C1qtnf1*, *Ube2v1* and *HS8st2* was mostly correlated with other DEGs (Fig. S7C). Among them, *Id1* is associated with angiogenesis and vascular differentiation [32], while *C1qtnf1* is a marker of atherosclerosis in humans [33].

Gene Ontology (GO) analysis demonstrated that the respiratory chain was the major molecular event altered by ferroptosis inhibition (Fig. 6G). In the top ten signalling pathways enriched in Chord plot analysis, seven signalling pathways were associated with the mitochondrial respiratory chain complex (Fig. 6H). Gene set enrichment analysis (GSEA) demonstrated that the assemblies of mitochondrial complexes I and III/IV were inhibited in injured arteries from GPX4-KI mice (Fig. 6I). In addition to the mitochondrial respiratory chain, we noticed inhibition of the response to transforming growth factor-β1 (TGF-β1) and immune cell functions and promotion of histone demethylase, which was reported to be an SMC dedifferentiation suppressor [34] (Fig. S8A). Protein–protein-interaction analysis supported that the major module of DEGs was the mitochondrial respiratory chain (Fig. S8B). We noted that in addition to the genes for mitochondrial complex I, such as *mt-ND1* and *Ndufs1*, the genes *Sdhd* and *mt-CO3*, which are involved in mitochondrial complexes II and III, were also inhibited in GPX4-KI mouse arteries (Fig. 6J and Fig. S8C). These results indicate that ferroptosis might regulate SMC phenotype switch by modulating mitochondrial function.

Involvement of ferroptotic stress in mitochondrial oxidation, dynamics and hyperpolarization in dedifferentiated SMCs

We next determined the contribution of ferroptotic stress to mitochondrial function in dedifferentiated SMCs. NDUFS1, the conserved core subunit of mitochondrial complex I, was remarkably induced in dedifferentiated SMCs but suppressed by the ferroptosis inhibitor Fer-1 (Fig. 7A). Similar change patterns in the protein expression of NADH dehydrogenase 1 and cytochrome C were observed (Fig. 7B). In accordance, the boosted mitochondrial complex I activity in dedifferentiated SMCs was significantly reduced by Fer-1 (Fig. 7C). We used the Seahorse metabolic flux analysis system to monitor the oxygen consumption rate (OCR) and extracellular acidification rate (ECAR) in dedifferentiated SMCs. As shown in Fig. 7D, the dedifferentiated SMCs displayed higher OCRs and ECARs (red curves), suggesting that there was a higher energy demand within these cells. Fer-1 treatment partially lowered OCR and ECAR values (blue curve). The basal OCR, maximum OCR, spare respiratory capacity (SRC), ATP production, basal ECAR and maximum ECAR were significantly reduced by Fer-1 treatment in dedifferentiated SMCs (Fig. 7E). However, the nonmitochondrial OCR and coupling efficiency did not differ between the two groups of SMCs (Fig. 7E). In line with these findings, the mitoSOX fluorescence study showed that the boosted mitochondrial ROS production in dedifferentiated SMCs was decreased by Fer-1 (Fig. 7F). The phosphorylation of the mitochondrial fission marker dynamin-related protein 1 (Drp1) was increased, while the mitochondrial fusion marker mitofusin 2 (Mfn2) was decreased in dedifferentiated SMCs, both of which were abolished by Fer-1 treatment (Fig. 7G). These results suggest that blockade of ferroptotic stress may impact mitochondrial dynamics and number. As expected, the MitoTracker Green fluorescence assay showed that the mitochondrial number in dedifferentiated SMCs was increased, while Fer-1 abolished this change (Fig. 7H). A fluorescence assay with TMRE, a voltage-sensitive fluorescent probe that accumulates primarily in polarized mitochondria, showed remarkable mitochondrial hyperpolarization in dedifferentiated SMCs, which was prevented by Fer-1 (Fig. 7I). Together, these findings suggest that ferroptotic stress facilitates SMC dedifferentiation by blocking mitochondrial dysfunction.

CuATSM impedes SMC phenotype switch, neointimal formation and vascular inflammation in mice

Copper-diacetyl-bis^{N4}-methylthiosemicarbazone (CuATSM), a neutral and lipophilic compound (Fig. S9A) used for positron emission tomography (PET) imaging [35, 36], was recently proven to be a potent ferroptosis inhibitor [37, 38]. Interestingly, CuATSM has shown good tolerance and low toxicity in clinical trials for ALS [39]. We used this agent to explore the translational potential of ferroptosis inhibition in wire-injured mice with arterial remodelling. The body weight, blood pressure, and plasma lipid levels were not significantly different between the vehicle and CuATSM-treated groups before and after injury (Table S6). CuATSM reduced ferroptotic biomarkers in neointima tissue (Fig. S9B). As expected, this intervention successfully reduced the neointimal area (Fig. 8A). Immunoblotting analysis demonstrated that CuATSM treatment inhibited SMC proliferative markers (Cyclin D1 and PCNA) and synthetic markers (OPN and vimentin) but increased the SMC contractile markers Calponin-1 and transgelin in injured arteries of mice (Fig. 8B). Similar effects of CuATSM treatment on the mRNA levels of proliferative markers (*Ccnd1 and Pcna*), promigration markers (*Mmp2* and *Mmp9*) and contractile markers (*Cnn1* and *SM22α*) were observed (Fig. S9C). In addition, CuATSM treatment significantly lowered the protein expression of proinflammatory factors within the neointimal tissue (Fig. 8C). These findings indicated that CuATSM impedes SMC phenotype switch, neointimal formation and vascular inflammation in mice.

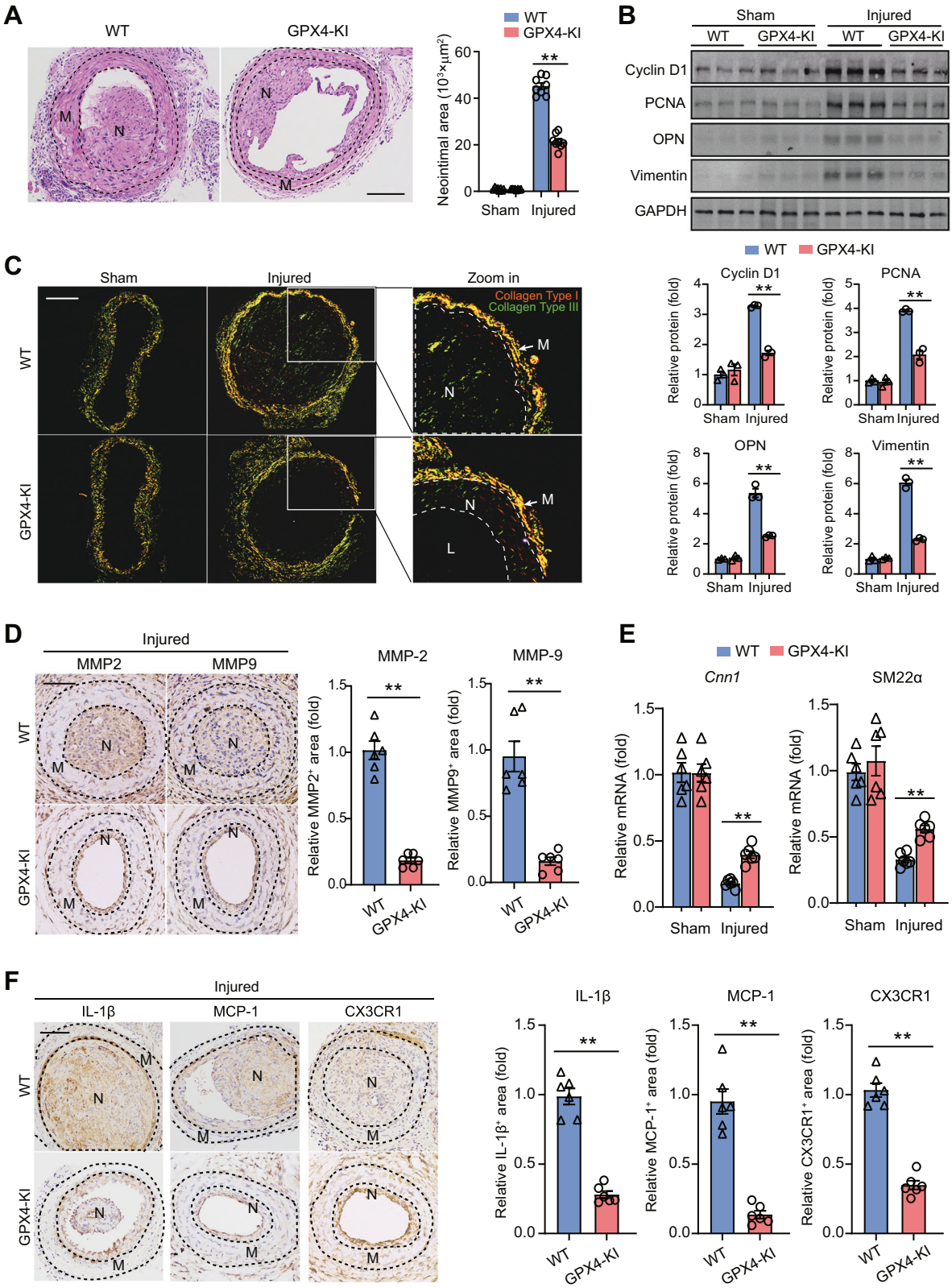

DISCUSSION

Recently, it has become clear that SMCs are more plastic than previously recognized and can dedifferentiate from the contractile phenotype to proliferative and synthetic phenotypes. Moreover, SMCs could elicit phenotypes resembling foam cells, macrophages, mesenchymal stem cells and even osteochondrogenic cells in the pathogenesis of CVDs [1–3]. We previously showed that proinflammatory factors are also implicated in SMC fate regulation [40–42]. It is generally believed that RCD, including apoptosis, necroptosis, autophagy-induced cell death, NETosis,

Fig. 4 Knockin of GPX4 protects against SMC phenotype switch and neointima formation in mice. A H & E staining showing the neointimal hyperplasia in wild-type (WT) and GPX4-knockin (KI) mice after wire-injury. $n = 8$ biological replicates per group. N, neointima; M, media. Scale bar, 100 μm. **B** Representative images and quantitative analyses of SMC proliferative markers (Cyclin D1 and PCNA) and synthetic markers (OPN and vimentin) in neointimal tissues from arteries of WT and GPX4-KI mice with Sham-operation and wire-injury. n = 3 biological replicates per group. **C** Evaluation of collagen fibres using Picrosirius staining under Polarization microscopy in neointimal tissues from arteries of WT and GPX4-KI mice with Sham-operation and wire-injury. The type I collagen fibres (orange) and type III collagen fibres (green signal) were clearly observed. N, neointima; M, media; L, lumen. Scale bar, 100 μm. **D** Representative immunohistochemistry images and quantitative analyses of SMC migration markers MMP2 and MMP9 in neointimal tissues. MMP2 and MMP9 were detected mainly in neointimal tissue but not arterial media layer. $n = 6$ biological replicates per group. Scale bar, 100 μm. N, neointima; M, media. **E** Quantitative PCR analyses of *Cnn1* and *SM22α* in arteries of WT and GPX4-KI mice with Sham-operation and wire-injury. $n = 6$ biological replicates per group. **F** Representative images and quantitative analyses of pro-inflammatory factors (IL-1β, MCP1 and CX3CR1) in neointimal tissues from arteries of WT and GPX4-KI mice with Sham-operation and wire-injury. $n = 6$ biological replicates per group. Scale bar, 100 μm. N, neointima; M, media. IL-1β, interleukin-1β; MCP1, monocyte chemoattractant protein-1; CX3CR1, C-X3-C Motif Chemokine Receptor 1. Data expressed as mean ± SEM. GAPDH was used as a loading control in immunoblotting. Comparisons were performed with unpaired two-sided Student *t* test since test. The values in sham group were not included for comparison. $^{*}P < 0.05$, $^{**}P < 0.01$.

ferroptosis, etc., are opposite mechanisms to cell proliferation [43]. Among RCD, apoptosis is the most well studied in CVDs with SMC phenotype switch by inhibiting neointima formation [4–6]. However, we know little about other types of RCD in SMC homeostasis maintenance.

In the present study, we examined the activation of ferroptosis-related signalling markers in dedifferentiated SMCs in vitro and in vivo. Notably, a comprehensive activation of the pro-ferroptotic phenotype was observed in the neointimal tissue of arteries from the mouse model and patients as well as in dedifferentiated SMCs stimulated by PDGF-BB. However, we did not observe real 'cell death' in the arteries with neointimal hyperplasia using the TUNEL assay or flow cytometry with the 7-AAD probe, which suggests that ferroptosis does not occur in parallel. This seems paradoxical, as these pro-ferroptotic stresses did result in a lethal outcome on SMC survival; however, they fuel the dedifferentiation of SMCs. This speculation is supported by our further findings in vivo and in vitro. Our findings are consistent with a previous study showing that lipid peroxidation inhibits phosphatase activity and increases PDGF-BB-induced PDGF receptor signalling [44], which may underlie our observation that pro-ferroptotic stress promoted the PDGF-BB-induced proliferation of SMCs in culture. Interestingly, we also observed that the ferroptosis inducer RSL-3 directly triggered SMC dedifferentiation in the absence of PDGF-BB. This finding supports previous works showing that the key nodes in ferroptosis regulatory signalling, such as DHODH [45], ALOX15 [46] and PUFA [47], may also regulate cell differentiation and dedifferentiation.

While many studies have demonstrated that activation of pro-ferroptotic signalling factors, such as inactivation of GPX4, DHODH, and ferroportin [48], as well as upregulation of ACSL4, ALOX12/15, PRMT4 [49], USP11 [50], and p53 [51], leads to ferroptosis, ferroptotic stress does not necessarily lead to irreversible cell death. Previously, ferroptotic stress was reported to promote a transient inflammatory state in proximal tubular cells, which made the cells more vulnerable to ferroptotic stress [52]. Ferroptotic stress increased cyst growth, whereas ferroptosis inhibition delayed cyst growth [53]. These results suggest that ferroptotic stress governs cellular identity and plasticity in epithelial cells in addition to triggering cell death. Our results extend the role of ferroptotic stress in cellular identity and plasticity in the nonepithelial lineage. It seems that activated SMCs are resistant to pro-ferroptotic stress, which might be associated with extensive downregulation of polyunsaturated ether phospholipids [54]. A possible explanation is that the anti-lipid peroxidation system has redundancy in the proliferated SMCs. Another explanation is that some key regulators of ferroptotic signalling may be multifunctional molecules beyond ferroptosis. For example, solute carrier family 7 member 11 (SLC7A11), a subunit of the glutamate-cystine antiporter System XC- with potent inhibition of ferroptosis [20, 55], plays a detrimental role in diabetic wound healing by suppressing efferocytosis [56].

Our findings established a molecular link between ferroptotic stress, mitochondrion and SMC phenotype switch. Mitochondria are central nodes of ferroptosis that dominate both ferroptotic and antiferroptotic mechanisms [57]. Most ferroptotic-related factors are associated with mitochondria. GPX4 localizes to mitochondria to exert its anti-ferroptosis action. Mitochondria also mediate cysteine deprivation-induced ferroptosis [15]. The mitochondrial enzyme DHODH, which catalyses the conversion of dihydroorotate to orotate, operates in parallel with mitochondrial GPX4 to inhibit ferroptosis in the mitochondrial inner membrane [13]. Activated and dedifferentiated SMCs grow faster, consume more oxygen for ATP production, and generate more mitochondrial ROS [58]. By using an unbiased transcriptome analysis, we found that ferroptosis inhibition remarkably suppressed the mitochondrial respiration chain, especially the subunits of mitochondrial complex I (*mt-ND1, mt-ND2, mt-ND6, Ndufs1, Ndufs2*, etc.). We also confirmed that altered mitochondrial metabolism was the central regulatory mechanism underlying the impact of ferroptotic stress on SMC phenotype switch. Seahorse experiments demonstrated that both oxidative phosphorylation and glycolysis were stimulated in dedifferentiated SMCs but suppressed by ferroptosis inhibition. Mitochondrial ROS were also increased in dedifferentiated SMCs and restrained by ferroptosis inhibition. These results are reasonable because enhanced mitochondrial ROS are required for the dedifferentiation of SMCs to promote SMC proliferative [59] and synthetic [60] phenotypes. In response to excessive energy demand, perturbation in mitochondrial dynamics, including fission and fusion, always occurs. Indeed, we observed that phosphorylation of Drp-1 was enhanced, while Mfn2 was reduced in dedifferentiated SMCs, both of which were prevented by ferroptosis inhibition. As previous studies have shown that Drp-1 promoted [61], whereas Mfn2 inhibited SMC phenotype switch and neointimal hyperplasia [62], our findings are apparently in line with these results and indicate that ferroptosis contributes to the abnormal mitochondrial dynamics.

Finding a new therapy that halts SMC dedifferentiation and maintains a contractile phenotype could prove promising in the treatment of vascular diseases. Numerous chemical ferroptosis inhibitors, such as Fer-1 and liproxstatin-1, have been developed. Among them, liproxstatin-1 is a good pharmacological inhibitor of ferroptosis in preclinical models and a lead compound for clinical translation. In this study, we evaluated the therapeutic potential of the PET imaging tracer CuATSM [35]. Recently, this agent was proven to be a potent ferroptosis inhibitor [37, 38]. Intriguingly, CuATSM protects against ALS and Parkinson's disease in animal models [63, 64] and has passed a phase I clinical trial in ALS patients (NCT02870634), suggesting that CuATSM may have good bioavailability, safety and tolerability. Currently, another phase 2 trial of CuATSM (NCT04082832) is ongoing to assess its efficacy [39]. We found

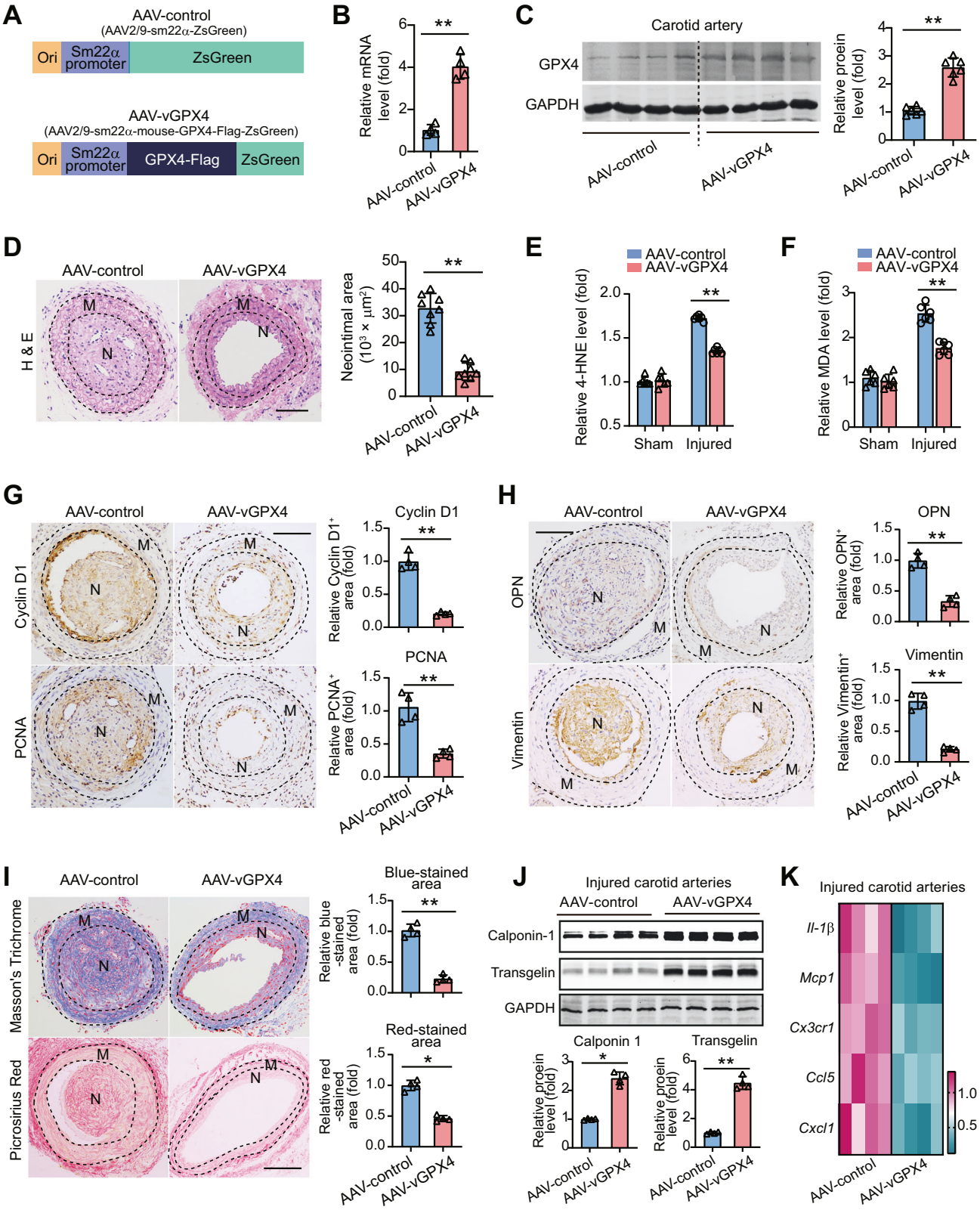

that treatment with CuATSM ameliorated SMC phenotype switch, neointimal hyperplasia and vasculature inflammation in the arteries of mice with wire injury. Coincidentally, CuATSM in PET imaging was found centrally located within lipid-rich SMCs of carotid atherosclerotic plaque in carotid stenosis patients [36]. This suggests that CuATSM could be developed as a potential therapeutic agent in SMC-related CVDs.

In conclusion, we demonstrate that ferroptotic stress orchestrates SMC plasticity by promoting mitochondrial metabolism and structural malfunction in arterial remodelling (Fig. 8D). Our

Fig. 5 Conditional SMC-specific gene delivery of GPX4 blocks SMC phenotype switch and retards neointima formation in mice. **A** Construction of a serotype 2/9 of adeno-associated virus (AAV2/9) carrying a coding sequence of mouse GPX4 (mGPX4) under SMC-specific SM22α promoter (AAV2/9-sm22α-mouse-GPX4-Flag-ZsGreen, referred as AAV-vGPX4). ZsGreen is a fluorescent protein used for tracing. The control AAV (AAV2/9-sm22a-ZsGreen, referred as AAV-control) was also constructed. **B**, **C** Gene delivery of GPX4 into carotid arteries was confirmed at mRNA (**B**) and protein (**C**) levels. $n = 4$–5 biological replicates per group. **D** H & E staining showing the neointimal hyperplasia in arteries form injured mice with administration of AAV-control or AAV-vGPX4. $n = 8$ biological replicates per group. N, neointima; M, media. Scale bar, 100 μm. **E**, **F** Levels of lipid peroxidation markers 4-HNE (**E**) and MDA (**F**) in arteries from sham-operated or injured mice with administration of AAV-control or AAV-vGPX4. n = 6 biological replicates per group. N, neointima; M, media. Scale bar, 100 μm. **G** Representative immunohistochemistry staining of SMC proliferation markers Cyclin D1 and PCNA in arteries from injured mice with administration of AAV-control or AAV-vGPX4. $n = 6$ biological replicates per group. N, neointima; M, media. Scale bar, 100 μm. **H** Representative immunohistochemistry staining of SMC synthetic markers OPN and vimentin in arteries from injured mice with administration of AAV-control or AAV-vGPX4. $n = 6$ biological replicates per group. N, neointima; M, media. Scale bar, 100 μm. **I** Representative Masson's Trichrome and Picrosirius Red staining of collagen fibre in arteries from injured mice with administration of AAV-control or AAV-vGPX4. The collagen fibres were blue in Masson's Trichrome staining and red in Picrosirius Red staining. $n = 6$ biological replicates per group. N, neointima; M, media. Scale bar, 100 μm. **J** Immunoblotting analysis of SMC contractile markers Calponin-1and transgelin in arteries from injured mice with administration of AAV-control or AAV-vGPX4. $n = 4$ biological replicates per group. Data expressed as mean ± SEM. GAPDH was used as a loading control in immunoblotting. Comparisons were performed with unpaired two-sided Student *t* test since the test. The values in sham group were not included for comparison. $^{*}P < 0.05$, $^{**}P < 0.01$.

findings suggest a potential link between ferroptosis and SMC dedifferentiation during arterial remodelling and indicate that a clinical candidate compound, CuATSM, is a promising therapeutic tool for the treatment of SMC phenotype switch-associated CVDs.

MATERIALS AND METHODS

Animals

Wild type 8-week-old control mice (C57BL/6) were purchased from Sino-British SIPPR/BK Lab Animal Ltd. (Shanghai, China). The knockin mice carrying GPX4 at the ROSA26 site (project No. KICMS181221LY4) was produced by Cas9/CRISPR-mediated genome editing (Cyagen Biosciences, Santa Clara, CA, USA) as described previously [31]. For the generation of R26-GPX4 mice, the "CAG-mouse GPX4 cDNA (NM_008162.3)-polyA" cassette was inserted into insurer 1 of ROSA26 under the guidance of gDNA (gDNA, GGCAGGCTTAAAGGCTAACCTGG). The GRNA was injected into fertilized mouse eggs in conjunction with the mouse ROSA26 gene, mouse DNA containing the mouse GPX4 gene, and Cas9 mRNA to produce targeted knockout offspring. Identification of F0-originated animals by PCR followed by sequence analysis (PCR Primers: Forward, 5′-AAAGATCGCTCTC-CACGCCCTAG-3′; Reverse, 5′-AGATGTACTGCCAAGTAGGAAAGTC-3′). Successfully knockin of the GPX4 allele was confirmed by primer sequencing as follows: Primer 1, 5′-CACTTGCTCTCCCAAAGTCGCTC-3′; Primer 2, 5′-ATACTCCGAGGCGGATCA-CAA-3′ and the positive targeting was also identified by southern blotting. Positive mice were hybridized with WT mice to test germline propagation and F1 animal production was successfully established. The following primers were used for genotyping: Forward, 5′-ACCTTTCTGGGAGTTCTCTGCTG-3′; Reverse 1, 5′-TACTTGGCATATGATACACTTGA-3′; Reverse 3, 5′-TTGTGGTGTATGTAACTAATCTG-3′. These mice underwent reverse hybridization with C57BL/6J mice for at least six generations. During animal experiments, the genotypes of all the mice studied were known to researchers. No predetermined mouse selection criteria were used other than sex and age. Animals were randomly grouped and assigned by technicians who were blind to the animal's appearance or other characteristics. All mice were housed under 12 h light/dark cycle and had free access to food and water. All operations in mice were approved by the Animal Care and Use Committee of our institution and followed the Principles of Laboratory Animal Care published by the National Institutes of Health and ARRIVE guidelines.

Human artery samples

Carotid artery from underwent carotid endarterectomy (CEA) and normal internal mammary artery (IMA) used for coronary artery bypass graft surgery were obtained from Department of Cardiac Surgery, Shanghai Tenth People's Hospital affiliated to Tongji University School of Medicine, Shanghai, China. The clinical characteristics were listed in Supplemental Table 1. For the use of human specimens, this study was approved and conducted in accordance with the requirements of the Ethics Committee of Shanghai Tenth People's Hospital (No. SHSY-IEC-KY-4.0/18-182/01). All participants give written informed consent.

Culture of human and mouse SMCs

Primary human carotid artery SMCs were obtained from the arteries from abovementioned patients. The fresh vessels were immediately cleaned of adipose and connective tissue and placed in an enzymatic solution (1 mg/ml collagenase II) for 30 min and transferred to serum-free medium, cleaned for adventitia under dissection stereoscope. The vessels were placed in an enzymatic solution (1 mg/ml collagenase and 0.25 mg/ml elastase) for an additional 1 h. After that, the partially digested tissue with enzyme solution was transferred into a 15 ml conical tube and gently triturate with a flame-polished glass pipette. The mixture was centrifuged at 1000 rpm for 5 min and the supernatant was discarded. The dissociated cells were resuspended in 2–3 ml of culture medium. Experiments were performed using human SMCs between passages 3 and 8. Mouse vascular smooth muscle cell line (MOVAS) obtained from American Type Culture Collection (ATCC) were used for cell biochemical experiments. The cells were cultured in DMEM medium (Gibco, MA, USA) containing 10% foetal bovine serum (FBS, 10099141, Gibco, MA, USA), and 1% penicillin-streptomycin (15140122, Gibco, MA, USA). Cells were maintained at 37 °C in a humidified environment with 5% CO_2.

Wire-induced arterial injury model and tissue sampling

Arterial injury model was induced as described previously [42]. For all surgical procedures, the 8-10-week-old mice were anesthetized by intraperitoneal injection with pentobarbital sodium (50 mg/kg). Surgery was carried out using a dissecting microscope (SMZ-800, Nikon, Tokyo, Japan). A guide wire (0.38 mm in diameter) was inserted into the left common carotid artery of mice. The wire was left in place for 1 min to denude and dilate the artery. Carprofen (5 mg/kg) was used for analgesia, administered subcutaneously daily for 3 days following surgery. For tissue sampling, the mice were anesthetized with sodium pentobarbital (50 mg/kg, intraperitoneal) 28 days after guidewire injury. The lesioned common carotid artery was carefully dissected, washed twice with ice-cold PBS solution, and then stored at −80 °C or fixed with 10% formalin for further examination.

Mouse blood pressure measurement

Non-invasive tail blood pressure was measured as in our previous studies [40, 65]. Mice were placed in the restraint corridor and allowed at least 30 min of acclimation. A quiet and dark environment was maintained to ensure reliable measurements within the parameters of blood pressure. Tuff-based tail monitor (NIBP200A, Alcbio, Shanghai) was used to record tail blood pressure. The blood pressure of each mouse was tested for 6 consecutive times to calculate the mean value.

SMC dedifferentiation and treatment

To activate dedifferentiation of SMCs, PDGF-BB (final concentration 20 ng/ml, #315-18, PeproTech) was added into the culture medium to stimulate SMC for 48 h. For inhibition of ferroptosis in SMCs, ferrostain-1 (final concentration 1 μM, #S9243, Selleck) was added into the culture medium.

CCK8 assay

Cell survival rates were estimated by the CCK-8 assay (Dojindo, Tokyo, Japan). Approximately 10^4 cells were seeded in 96-well plates with 100 μl of medium per well. After 24 h of culture, ferrostain-1 treatment or transfection of plasmids were continued. Each well was incubated with 10 μg of CCK-8 solution for 1 h in the dark before measuring absorbance at 450 nm with a microplate reader.

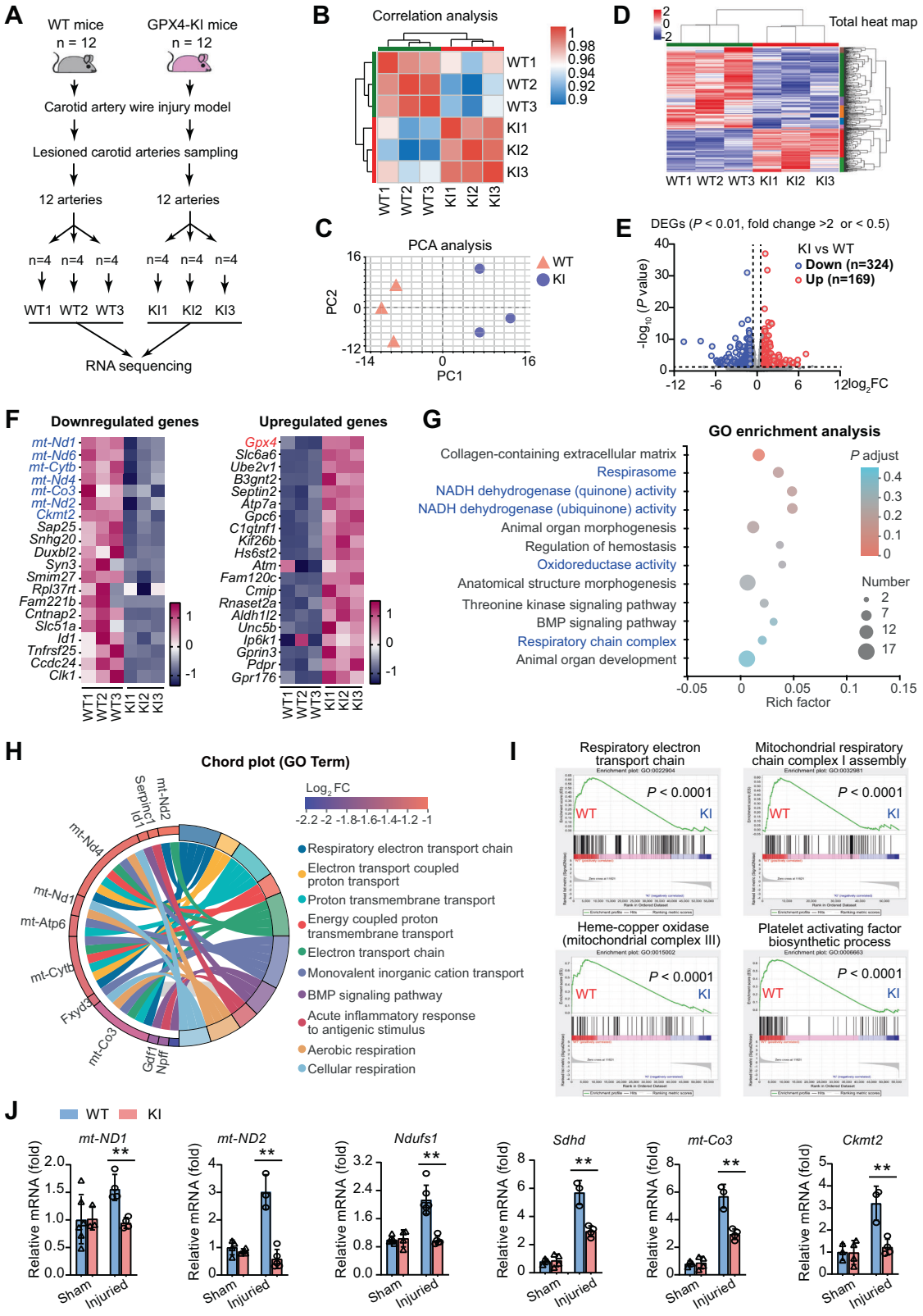

Lipid peroxidation assay

For detecting the lipid peroxidation levels, cells were seeded on 24-well plates and incubated for attachment. Cells were treated with 2.5 μM BODIPY$^{581/591}$ C11 dye (Invitrogen, Carlsbad) for 15 min in the cell incubator. Then, the cells were washed with 1X icecold PBS and trypsinized to obtain a single-cell suspension. Lipid peroxidation levels were detected using flow cytometer (FACS Calibur, BD Bioscience, MD) or under IX73 fluorescence microscope (Olympus, Tokyo, Japan). The levels of MDA (#700870, Cayman Chemical, Arbor, MI) and 4-HNE (#E4645-100, BioVision, Milpitas, CA) in artery tissue or cells were determined with commercial kits according to the manufacturer's instructions.

Fig. 6 Transcriptomic study identifies a comprehensive inhibition on mitochondrial respiratory metabolism in neointimal tissue of GPX4-knockin mice. A A schematic representation showing the comparative transcriptomic study using RNA-sequencing between carotid arteries from WT and GPX4-KI (referred as KI) mice after wire-injury. To get enough amount RNA for library construction, twelve lesioned carotid arteries from each group were randomly pooled into three samples respectively. The data were analyzed using bioinformatics to obtain differentially expressed genes (DEGs). **B** Correlation analysis of RNA-sequencing results in six samples from two groups. **C** Principal component analysis (PCA) of six samples from two groups. **D** Total heat map showing the differentially expressed genes identified by RNA-seq between WT and KI mice aortae. **E** Volcano plot showing the 169 upregulated and 324 downregulated DEGs (criteria: $P < 0.01$, fold change >2 or <0.5) in injured arteries from KI mice compared with those from WT mice. **F** Heatmap showing the top 20 downregulated and upregulated DEGs after being further screened with criteria with P adjust < 0.001. A plenty of mitochondrial genes were noted in the top 20 downregulated genes. **G** Gene Ontology (GO) analysis of the DEGs showing the enriched mainly altered molecular events. Respirasome, NADH dehydrogenase activity and respiratory chain complex were noted. **H** Chord plot analysis of the DEGs showing that seven of the top 10 enriched signalling pathways were mitochondrial-related biological functions. **I** Gene Set Enrichment Analysis (GSEA) analysis demonstrating the inhibited respiratory electron transport chain, assemblies of mitochondrial complex I and III/IV (Heme-copper oxidase) and platelet activating factor biosynthetic process in injured arteries of KI mice compared with those of WT mice. **J** Quantitative PCR analyses were applied to confirm the RNA-sequencing results of mRNA expression change in mitochondrial genes (*mt-ND1, mt-ND2, Ndufs1, Sdhd, mt-Co3* and *Ckmt2*) in sham-operated (Sham) and injured arteries of WT and KI mice. Data expressed as mean ± SEM. Comparisons were performed with unpaired two-sided Student t test. The values in sham group were not included for comparison. $^{*}P < 0.05$, $^{**}P < 0.01$.

5-ethynyl-2-deoxyuridine (EdU) assay

In the EdU assay, cells were seeded into 24-well plates (100 μl well; 2×10^5 cells/well) overnight. After synchronization by serum starvation, cells were transfected with PDGF-BB (20 ng/ml) or plus Fer-1 (2 μM) for 48 h. EdU assays were performed using the EdU Cell Proliferation Assay Kit (#C10646, Invitrogen) according to the instructions. Hoechst 33342 was added into the cells to stain nuclei. The cells were visualized using a laser scanning confocal microscope BX53 (Olympus, Tokyo, Japan). EdU positive cells (red) were counted by Image J software (NIH).

Transwell migration assay

Transwell migration assays were performed using transwell inserts (#3464, Corning, USA) with 8 μm pore size filters. Seed 8×10^4 cells in serum-free medium into the upper chamber of the transwell inserts and add complete medium to the lower chamber. After 36 h of incubation, cells were fixed and stained with crystal violet. Cells on the upper surface of the membrane were then wiped off, and cells on the lower surface were observed with an Olympus BX53 microscope. Four random fields of view were taken for counting purposes, and the average number of migrating cells was used as a measure of migratory capacity.

Wound healing test

When cells seeded in six-well plates reach confluence, a single scratch was performed using a sterile 10 μl pipette tip. Cells were then grown in FBS-free cultured medium alone (to rule out potential effects of FBS on cell migration) or in medium containing PDGF-BB (20 ng/ml) or PDGF-BB plus Fer-1. Images of scratches were captured at 0 and 48 h using an inverted microscope BX53 (Olympus, Tokyo, Japan). The width of the scratches was analyzed using Image J software (NIH).

Quantitative PCR

Total RNA of tissues or cells was extracted with Trizol RNA Isolation Kit (Invitrogen). RNA quality was assessed using Nanodrop (Thermo Fisher Scientific) at 260/280 nm absorbance ratio. Available when the ratio was 1.8~2.0. After measuring the RNA concentration, reverse transcription was performed using One-Step gDNA Removal and cDNA Synthesis SuperMix (TransGen Biotech, China). Real-time quantitative PCR (qPCR) was performed using the BioRad CFX96 system (Bio-Rad Laboratories, Hercules, CA) and SYBR Premix Ex Taq Mixture (Takara, Tokyo, Japan). Each sample was assayed in duplicate and the housekeeping gene 18S rRNA was used as a reference gene for normalization. Primer sequences were found in Supplementary Table 5. Cycle threshold (CT) values were recorded and fold changes of genes were quantified using the $^{\Delta\Delta}$CT method.

Immunoblotting

Tissue was lysed at 4 °C in a homogenizer with lysis buffer containing 1% Triton-X-100 and a protease and phosphatase inhibitor cocktail (Sigma). The cultured cells were lysed directly on ice after adding buffer. Proteins were run on 8–12% SDS-PAGE gels at room temperature for 1.5 h at 120 V. The gels were then transferred to a nitrocellulose membrane (200 mA, 1 h) in an ice-water bath. Block the membrane with 5% non-fat milk dissolved in PBST buffer (0.5% v/v Tween-20 in PBS buffer) for 2 h at room temperature. Wash membrane three times (5 min each) with PBST and incubate with primary antibodies (anti-ACSL4, #sc-365230, Santa Cruz Biotechnology; anti-GPX4, #ab125066, Abcam; anti-ALOX15, #PA5-15065, Invitrogen; anti-TFR, #10084-2-AP, Proteintech; anti-MDA, #ab6463, Abcam; anti-4-HNE, #ab46545, Abcam; anti-Cyclin D1, #sc-450, Santa Cruz Biotechnology; anti-PCNA, # BM0104, Boster; anti-MMP2, # 10373-2-AP, Proteintech; anti-MMP9, # 10375-2-AP, Proteintech; anti-vimentin, #sc-6260, Santa Cruz Biotechnology; anti-OPN, #22952-1-AP, Proteintech; anti-Calponin-1, #ab46794, Abcam; anti-transgelin, #ab14106, Abcam; anti-mt ND1, #ab181848, Abcam; anti-NDUFS1, #sc-271510, Santa Cruz Biotechnology; anti-Cytochrome C, #ab133504, Abcam; anti-Drp1, # ab184247, Abcam; anti-p-Drp1, #3455, Cell Signalling Technology; anti-Mfn2, #9482, Cell Signalling Technology; anti-VDAC1, #sc-390996, Santa Cruz Biotechnology; anti-GAPDH, #60004-1, Proteintech) overnight at 4 °C. Primary antibodies dilution ranged from 1:1000 to 1:5000. After washing, the membrane was incubated with a secondary antibody conjugated to IRDye® 800CW (Li-Cor Biosciences). Images were captured using the Odyssey system (Li-Cor Biosciences) and analyzed using Image J software (NIH).

Immunohistochemistry

Lesioned carotid artery was fixed in 4% formaldehyde for 30 min and then dehydrated in 30% sucrose. After paraffin embedding, sections (8 μm) were blocked in 5% goat serum for 4 h at room temperature. Sections were incubated with primary antibodies (anti-ACSL4, #sc-365230, Santa Cruz Biotechnology; anti-TFR, #10084-2-AP, Proteintech; anti-ALOX15, #PA5-15065, Invitrogen; anti-MDA, #ab6463, Abcam; anti-4-HNE, #ab46545,Abcam; anti-Cyclin D1, #sc-450, Santa Cruz Biotechnology; anti-PCNA, # BM0104, Boster; anti-CX3CR1, #ab245248, Abcam; anti-MMP2, # 10373-2-AP, Proteintech; anti-MMP9, # 10375-2-AP, Proteintech; anti-IL-1β, #sc-12742, Santa Cruz Biotechnology; anti-MCP-1, #66272-1-Ig, Proteintech) overnight at 4°C, followed by peroxidase-conjugated secondary antibody for 1 h. 3,3-Diaminobenzidine was used as a chromogenic enzyme substrate before counterstaining with hematoxylin. The sections were imaged with a digital microscope (Leica Microsystems, Berlin, Germany). All image analysis were performed using Image J software (NIH). All immunohistochemical quantifications were performed by two independent pathologists in a blinded manner.

Mitochondrial assays

For isolation of cytosolic and mitochondrial fractions, cells were prepared using a mitochondrial isolation kit (89874, Thermo Fisher Scientific) according to the manufacturer's instructions. The whole cell lysate was obtained using whole-cell extraction kit (ab113475, Abcam). Mitochondrial complex I activity was measured using a commercial kit from Abcam (ab109721). For mitochondrial ROS determination, cultured SMCs were placed on confocal dish (Corning, CA) and incubated with MitoSOX Red probe (Invitrogen) for 30 min in the dark at 37 °C. For evaluation of mitochondrial number, cultured SMCs were incubated with Mito-track-Green probe (Invitrogen) for 30 min in the dark at 37 °C. For evaluation of mitochondrial membrane potential (Δψm), cultured SMCs were incubated with a membrane potential-sensitive tetramethylrhodamine methyl ester (TMRE probe, Invitrogen) and a Tubulin-Tracker Green probe (Invitrogen) for 30 min in the dark at 37 °C. In these assays, Hoechst 33342 was used to stain nuclei. The cells were observed with a Zeiss laser confocal microscope (LSM 800).

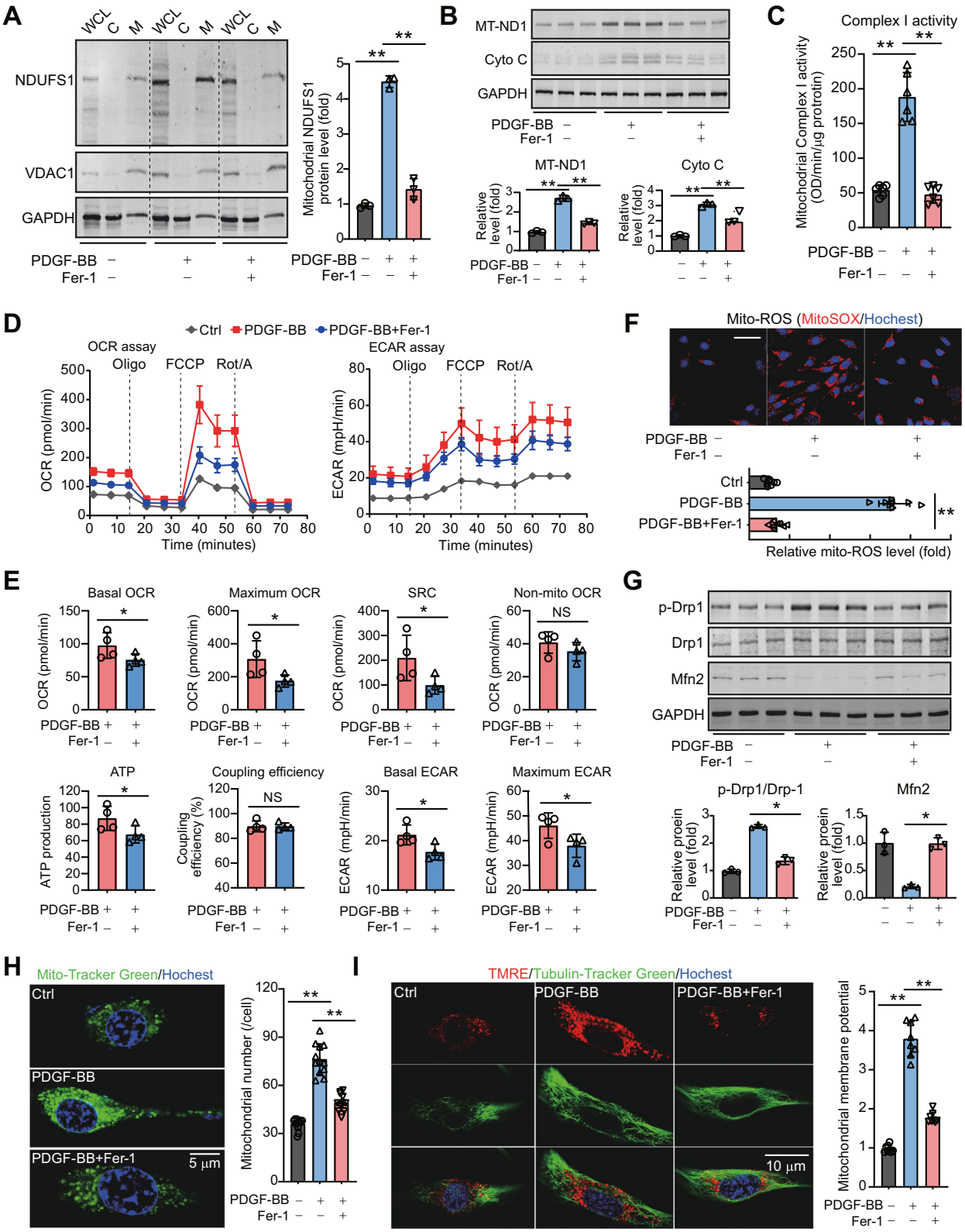

Seahorse XF metabolic analysis

Oxygen consumption rates (OCR) and extracellular acidification rate (ECAR) were measured using an XF-96 Extracellular Flux Analyzer (Seahorse Bioscience). SMCs were seeded on Seahorse 96-well assay plates at 5000 cells per well and tested in XF assay medium containing 5 mM glucose, 4 mM pyruvate, and 2 mM L-glutamine. OCR was measured in basal conditions and in response to 2 μM oligomycin (ATP synthase inhibitor), 3 μM fluorocarbonyl cyanide phenylhydrazone (FCCP, uncoupler), 2 μM rotenone (Complex I inhibitor) and 2 μM antimycin A (Complex III inhibitor). ECAR was measured during the entire experiment. Analysis was performed using Seahorse Wave Desktop Software (Agilent).

Fig. 7 Inhibition of ferroptotic stress corrects mitochondrial ROS generation, dysregulated mitochondrial dynamics and mitochondrial hyperpolarization in dedifferentiated SMCs. A Immunoblotting analysis of mitochondrial complex I subunit NADH:ubiquinone oxidoreductase core subunit S1 (NDUFS1) in whole cell lysate (WCL), cytoplasmic fraction (C) and mitochondrial fraction (M) of SMCs. PDGF-BB was used to induce SMC dedifferentiation. Voltage-dependent anion-selective channel 1 (VDAC1) was used as a loading control of mitochondrial fraction, while GAPDH was used as a loading control of whole cell lysate. **B** Immunoblotting analysis of mitochondrial complex I subunit mitochondrial NADH-ubiquinone oxidoreductase chain 1 (MT-ND1) and mitochondrial complex III/IV subunit cytochrome C (Cyto C) in dedifferentiated SMCs. $n = 3$ biological replicates per group. **C** Activity of mitochondrial complex I in dedifferentiated SMCs. $n = 6$ biological replicates per group. **D** Seahorse metabolic flux analyses showing the curves of oxygen consumption rates (OCR) and extracellular acidification rate (ECAR) in dedifferentiated SMCs. $n = 4$ biological replicates per group. **E** Influence of Fer-1 on basal OCR, maximum OCR, spare respiratory capacity (SRC), non-mitochondrial OCR, ATP production, coupling efficiency, basal ECAR and maximum ECAR in dedifferentiated SMCs. $n = 4$ biological replicates per group. **F** Mitochondrial ROS was assessed by MitoSOX probe fluorescence intensity. Hochest was used to stain nuclei. $n = 8$ biological replicates per group. **G** Mitochondrial dynamics was evaluated using immunoblotting analysis of mitochondrial fission marker (Drp1 and phosphorylated Drp1 [p-Drp1]) and mitochondrial fusion marker Mfn2. $n = 3$ biological replicates per group. **H** Confocal microscopy analysis of mitochondrial number in dedifferentiated SMCs with Mito-tracker-green probe staining. For the measurement, ~15 SMCs per well were observed to obtain the mitochondrial number in each culture well. $n = 10$ wells per group. **I** Confocal microscopy analysis of mitochondrial membrane potential ($\Delta\psi m$) in dedifferentiated SMCs with immunofluorescence of tetramethylrhodamine ethyl ester (TMRE), a probe dependent to $\Delta\psi m$. Tubulin-tracker and Hoechst probes were used to stain SMC cytoskeleton and nuclei respectively. Data expressed as mean ± SEM. Comparisons were performed with unpaired two-sided Student *t* test (two groups) or one-way ANOVA followed by Tukey-hoc test (three groups). $^{*}P < 0.05$, $^{**}P < 0.01$.

Histology staining, Picrosirius Red staining and polarization microscopy

Hematoxylin-eosin staining (H & E), Masson's trichrome, Picrosirius Red staining were used to evaluate the degree of intimal hyperplasia and collagen-related fibrosis, respectively. Common carotid artery sections (8 μm) were stained with standard procedures as reported in our previous studies [42, 66]. Picrosirius Red staining was analyzed using polarization microscopy as in our previous study [67].

Prussian blue stain

To further characterize arterial ferroptosis, iron deposits were stained with Prussian blue (PB). PB stains hemosiderin and, to a lesser extent, ferritin deposits. The stain consisted of equal parts 20% hydrochloric acid (v/v) and 10% potassium ferrocyanide (w/v, Sigma). Glass-fixed sections were stained with PB for 20 min, washed in running water for 1 min, and counterstained with 0.5% aqueous nuclear fast red solution (Sigma) for 1 min.

RNA-sequencing

Transcriptomic study with RNA sequencing was performed as described previously [31]. Lesioned carotid arteries of WT and R26-GPX4 mice were obtained 28 days after wire injury, and total RNA was extracted. Total RNA was extracted from the tissue using TRIzol® Reagent according the manufacturer's instructions (Invitrogen) and genomic DNA was removed using DNase I (TaKara). Then RNA quality was determined by 2100 Bioanalyser (Agilent) and quantified using the ND-2000 (NanoDrop Technologies). Only high-quality RNA sample (OD260/280 = 1.8~2.2, OD260/230 ≥ 2.0, RIN ≥ 6.5, 28 S:18S ≥ 1.0, >1 μg) was used to construct sequencing library. RNA-seq transcriptome library was prepared following TruSeqTM RNA sample preparation Kit from Illumina (San Diego, CA) using 1 μg of total RNA. Shortly, messenger RNA was isolated according to polyA selection method by oligo(dT) beads and then fragmented by fragmentation buffer firstly. Secondly double-stranded cDNA was synthesized using a SuperScript double-stranded cDNA synthesis kit (Invitrogen, CA) with random hexamer primers (Illumina). Then the synthesized cDNA was subjected to end-repair, phosphorylation and 'A' base addition according to Illumina's library construction protocol. Libraries were size selected for cDNA target fragments of 300 bp on 2% Low Range Ultra Agarose followed by PCR amplified using Phusion DNA polymerase (NEB) for 15 PCR cycles. After quantified by TBS580, paired-end RNA-seq sequencing library was sequenced with the Illumina HiSeq xten/NovaSeq 6000 sequencer (2 × 150 bp read length).

For bioinformatics analyses, raw sequence reads were initially processed using FastP (Babraham Institute, Cambridge, UK) for quality control, and then adapter sequences and poor-quality reads were removed using Cutadapt. Quality-filtered reads were then mapped to mouse genome using STAR, and only the uniquely mapped reads were kept. Read counts were calculated using HTSeq-count. Differentially expressed genes were identified using R package DESeq2 (fold change ≥2 or <0.5, $p < 0.05$). Functional-enrichment analysis including GO and KEGG were performed to identify which DEGs were significantly enriched in GO terms and metabolic pathways at Bonferroni-corrected *P*-value ≤ 0.05 compared with the whole-transcriptome background. GO functional enrichment and KEGG pathway analysis were carried out by Goatools (https://github.com/tanghaibao/Goatools) and KOBAS (http://kobas.cbi.pku.edu.cn/home.do). The correlation data was calculated by using corrplot function and the graph was made by ggplot2 packages in R software.

The Raw RNA-sequencing data was deposited in NCBI Sequence Read Archive (SRA) database (No. PRJNA839930, https://www.ncbi.nlm.nih.gov/bioproject/PRJNA839930).

Adeno-associated virus (AAV) construction and administration

The AAV carrying GPX4 and negative control AAV vector were constructed and packaged by HanBio (Shanghai, China) as described previously. Briefly, the vector pHBAAV-SM22a-ZsGreen was selected for use in this study, and restriction endonuclease BamHI and HindIII was used for vector cleavage to obtain a purified linearized vector. The mouse GPX4 fragments were amplified using 2xFlash PCR MasterMix (Dye) kit according to the manufacturer's instructions. An HB infusionTM kit (Hanbio Biotechnology) was then used for the ligation of the linearized vector and mouse GPX4 fragments, according to the manufacturer's instructions, followed by transformation of DH5α competent cell (TIANGEN). After cultivating with LB medium in culture plates for 12–16 h, the bacterial solution was used for PCR identification with 2xHieff PCR Master MIX (Dye) kit (YEASON) according to the manufacturer's instructions and the amplified sequence was detected by Sanger Sequencing to verify the consistency with GPX4. The plasmid was extracted with TIANpure Mini Plasmid Kit (TIANGEN) according to the manufacturer's instructions. Finally, the extracted plasmid was co-transfected with Packaging plasmids (pAAV-RC and pHelper) into HEK-293T cells using LipofiterTM transfection reagent (HanBio) as per the manufacturer's instructions. After 72 h of transfection, the transfected HEK-293T cells were centrifuged and broken, and the supernatant was collected for virus purification using ViraTrap™ AAV Purification Maxiprep Kit (Biomiga). The titer is 1.6×10^{12} vg/mL. For gene delivery of GPX4 specifically in SMCs, the mice were administrated by AAV for twice. The first administration was achieved by direct micro-injection of virus (1×10^{11} vg per mouse) into the lumen of injured common carotid artery after wire-injury immediately for 20-min infection. Two weeks after wire-injury, mice were injected with the indicated virus (3×10^{11} vg per mouse) via tail vein.

Plasmid constructs and transfection

The pcDNA3.1 plasmid was purchased from Thermo Fisher Scientific (#V79520). The plasmids carrying mouse GPX4 was described previously [31]. The coding sequence of mouse GPX4 was subcloned into the pcDNA3.1 backbone. The pcDNA3.1 plasmid without the inserted DNA sequence was used as a control. Plasmids were extracted using the EndoFree Plasmid Maxi Kit (#12362, Qiagen, Germantown, MD). The plasmid was sequenced with T7 promoter primers to ensure sequence correctness. Purified plasmids were transfected into cells using Lipofectamine LTX reagent and PLUS reagent (Thermo Fisher Scientific, #15338100) whne cells were grown to 50–70% confluency in 12-well dishes and transfected with plasmid or control vector.

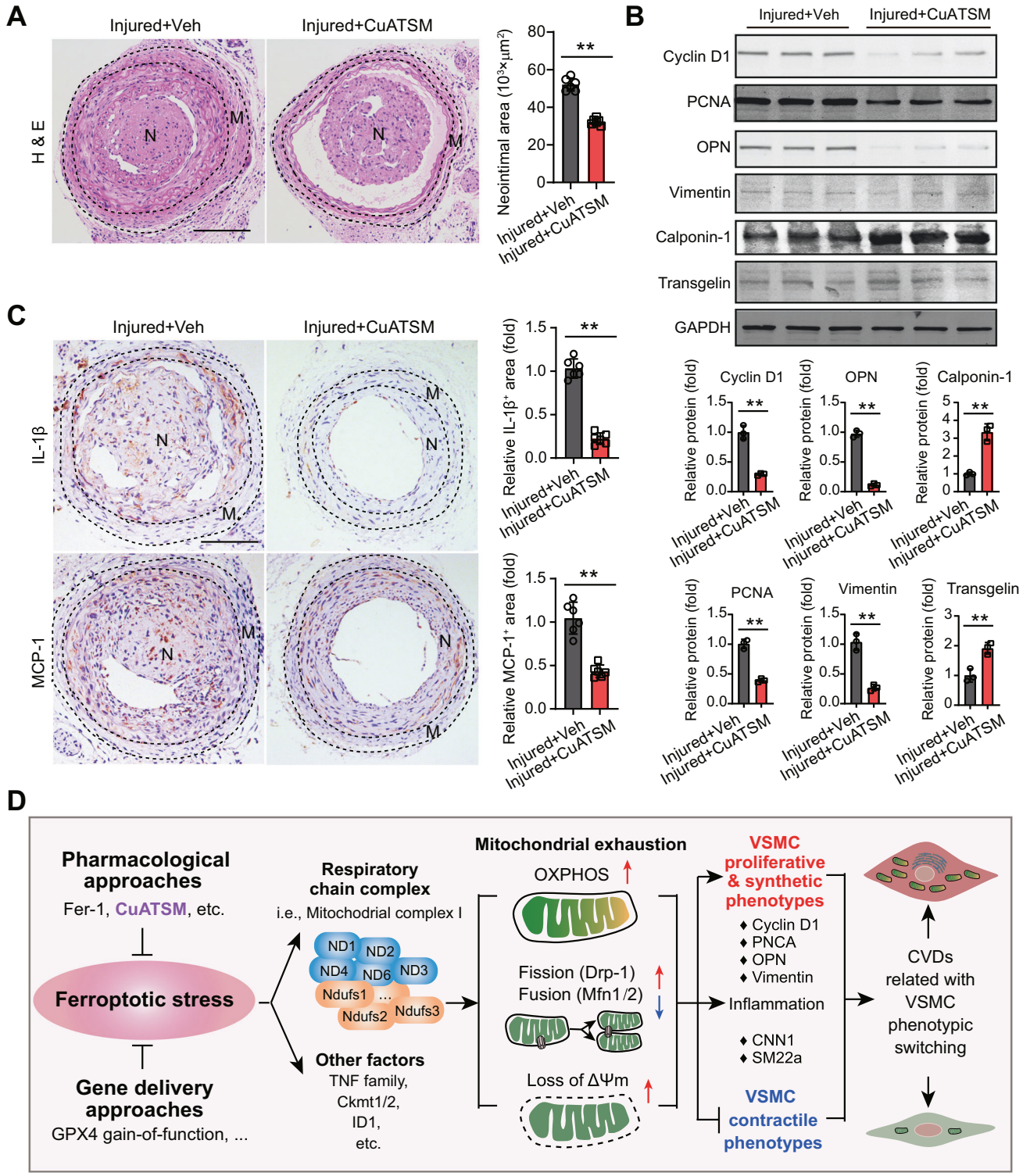

Fig. 8 CuATSM prevents SMC phenotype switch, neointimal hyperplasia and vascular inflammation by inhibiting ferroptotic stress in mice. A H & E staining showing the neointimal hyperplasia in carotid arteries mice at 28 days post injury treated with CuATSM (10 mg/kg, i.p., once per day) or same-volume vehicle control (Veh) for four weeks. $n = 6$ biological replicates per group. N, neointima; M, media. Scale bar, 100 μm. **B** Evaluation of SMC phenotype switch in injured arteries from CuATSM or vehicle-treated mice using immunoblotting analyses on molecular markers of proliferation (Cyclin D1 and PCNA), synthetic capacity (OPN and vimentin) and contractile capacity (Calponin-1 and transgelin). $n = 3$ biological replicates per group. **C** Evaluation of vascular inflammation in injured arteries from CuATSM or vehicle-treated mice using immunohistochemistry analyses on pro-inflammatory factors IL-1β and MCP-1. $n = 6$ biological replicates per group. **D** A working model showing a network that ferroptotic stress promotes SMC phenotypic switch in arterial remodelling by disrupting mitochondrial homeostasis, and suggests that targeted inhibition of ferroptotic stress using pharmacological or gene delivery approaches, is able to alleviate CVDs associated with SMC phenotype switch. Data expressed as mean ± SEM. Comparisons were performed with unpaired two-sided Student *t* test. $^{**}P < 0.01$.

Treatment of CuATSM

CuATSM was produced as descried previously [68]. ATSM stock solution was prepared by dissolving of ATSM (1 g, 3.8 mmol) powder in 1 mL of ethanol. The ethanolic solution of copper acetate (0.768 g, 3.8 mmol) was added dropwise. The colour of the solution changes from turbid white to brown red. The reaction mixture was fluxed at 60–70 °C for 4 h and refluxed overnight at room temperature. The solution was aliquoted and stored in a −20 °C freezer until use. For administration in mice, the stock solution of CuATSM was dissolved in DMSO solubilizer and further diluted with deionized water. The concentration of DMSO is 5% in the final solution. The CuATSM solution was injected intraperitoneally (5 mg/kg, once per day) for four weeks according to previous investigations [63, 69].

Statistical analysis

All results were presented as mean ± SEM. The distribution of data within all individual groups was verified by the Shapiro-Wilk test of normality. The statistical analysis was performed by Student's *t* test (two groups) or analysis of variance (ANOVA) followed by Tukey-hoc test (more than two groups). Sample sizes were based in standard protocols in the field. The number of animals/samples in each group is indicated in the figure legend. Unless otherwise stated, the statistical significance level was set at 0.05. All statistical analyses were performed using GraphPad Prism 8.

DATA AVAILABILITY

All data associated with this study are present in the paper or the Supplementary Materials. GO functional enrichment and KEGG pathway analysis were carried out by Goatools (https://github.com/tanghaibao/Goatools) and KOBAS (http://kobas.cbi.pku.edu.cn/home.do). The Raw data of RNA-sequencing was deposited in NCBI Sequence Read Archive (SRA) database (No. PRJNA839930).

REFERENCES

1. Durham AL, Speer MY, Scatena M, Giachelli CM, Shanahan CM. Role of smooth muscle cells in vascular calcification: implications in atherosclerosis and arterial stiffness. Cardiovasc Res. 2018;114:590–600.
2. Miano JM, Fisher EA, Majesky MW. Fate and state of vascular smooth muscle cells in atherosclerosis. Circulation. 2021;143:2110–6.
3. Melnik T, Jordan O, Corpataux JM, Delie F, Saucy F. Pharmacological prevention of intimal hyperplasia: a state-of-the-art review. Pharm Ther. 2022;235:108157.
4. Pollman MJ, Hall JL, Mann MJ, Zhang L, Gibbons GH. Inhibition of neointimal cell bcl-x expression induces apoptosis and regression of vascular disease. Nat Med. 1998;4:222–7.
5. Guo X, Chen KH, Guo Y, Liao H, Tang J, Xiao RP. Mitofusin 2 triggers vascular smooth muscle cell apoptosis via mitochondrial death pathway. Circ Res. 2007;101:1113–22.
6. Ostriker AC, Xie Y, Chakraborty R, Sizer AJ, Bai Y, Ding M, et al. TET2 protects against vascular smooth muscle cell apoptosis and intimal thickening in transplant vasculopathy. Circulation. 2021;144:455–70.
7. Dixon SJ, Lemberg KM, Lamprecht MR, Skouta R, Zaitsev EM, Gleason CE, et al. Ferroptosis: an iron-dependent form of nonapoptotic cell death. Cell. 2012;149:1060–72.
8. Yang WS, SriRamaratnam R, Welsch ME, Shimada K, Skouta R, Viswanathan VS, et al. Regulation of ferroptotic cancer cell death by GPX4. Cell. 2014;156:317–31.
9. Friedmann Angeli JP, Schneider M, Proneth B, Tyurina YY, Tyurin VA, Hammond VJ, et al. Inactivation of the ferroptosis regulator Gpx4 triggers acute renal failure in mice. Nat Cell Biol. 2014;16:1180–91.
10. Bersuker K, Hendricks JM, Li Z, Magtanong L, Ford B, Tang PH, et al. The CoQ oxidoreductase FSP1 acts parallel to GPX4 to inhibit ferroptosis. Nature. 2019;575:688–92.
11. Doll S, Freitas FP, Shah R, Aldrovandi M, da Silva MC, Ingold I, et al. FSP1 is a glutathione-independent ferroptosis suppressor. Nature. 2019;575:693–8.
12. Mishima E, Ito J, Wu Z, Nakamura T, Wahida A, Doll S, et al. A non-canonical vitamin K cycle is a potent ferroptosis suppressor. Nature. 2022;608:778–83.
13. Mao C, Liu X, Zhang Y, Lei G, Yan Y, Lee H, et al. DHODH-mediated ferroptosis defence is a targetable vulnerability in cancer. Nature. 2021;593:586–90.
14. Lee H, Zandkarimi F, Zhang Y, Meena JK, Kim J, Zhuang L, et al. Energy-stress-mediated AMPK activation inhibits ferroptosis. Nat Cell Biol. 2020;22:225–34.
15. Gao M, Yi J, Zhu J, Minikes AM, Monian P, Thompson CB, et al. Role of mitochondria in ferroptosis. Mol Cell. 2019;73:354–63.
16. Wang K, Zhang Z, Tsai HI, Liu Y, Gao J, Wang M, et al. Branched-chain amino acid aminotransferase 2 regulates ferroptotic cell death in cancer cells. Cell Death Differ. 2021;28:1222–36.
17. Zhang Y, Luo M, Cui X, O'Connell D, Yang Y. Long noncoding RNA NEAT1 promotes ferroptosis by modulating the miR-362-3p/MIOX axis as a ceRNA. Cell Death Differ. 2022;29:1850–63.
18. Wu Y, Jiao H, Yue Y, He K, Jin Y, Zhang J, et al. Ubiquitin ligase E3 HUWE1/MULE targets transferrin receptor for degradation and suppresses ferroptosis in acute liver injury. Cell Death Differ. 2022;29:1705–18.
19. Nguyen KT, Mun SH, Yang J, Lee J, Seok OH, Kim E, et al. The MARCHF6 E3 ubiquitin ligase acts as an NADPH sensor for the regulation of ferroptosis. Nat Cell Biol. 2022;24:1239–51.
20. Jiang L, Kon N, Li T, Wang SJ, Su T, Hibshoosh H, et al. Ferroptosis as a p53-mediated activity during tumour suppression. Nature. 2015;520:57–62.
21. Chen D, Chu B, Yang X, Liu Z, Jin Y, Kon N, et al. iPLA2beta-mediated lipid detoxification controls p53-driven ferroptosis independent of GPX4. Nat Commun. 2021;12:3644.
22. Ingold I, Berndt C, Schmitt S, Doll S, Poschmann G, Buday K, et al. Selenium utilization by GPX4 is required to prevent hydroperoxide-induced ferroptosis. Cell. 2018;172:409–22.e21.
23. Pedrera L, Espiritu RA, Ros U, Weber J, Schmitt A, Stroh J, et al. Ferroptotic pores induce Ca(2+) fluxes and ESCRT-III activation to modulate cell death kinetics. Cell Death Differ. 2021;28:1644–57.
24. Fang X, Wang H, Han D, Xie E, Yang X, Wei J, et al. Ferroptosis as a target for protection against cardiomyopathy. Proc Natl Acad Sci USA. 2019;116:2672–80.
25. Fang X, Cai Z, Wang H, Han D, Cheng Q, Zhang P, et al. Loss of cardiac ferritin H facilitates cardiomyopathy via Slc7a11-mediated ferroptosis. Circ Res. 2020;127:486–501.
26. Qin X, Zhang J, Wang B, Xu G, Yang X, Zou Z, et al. Ferritinophagy is involved in the zinc oxide nanoparticles-induced ferroptosis of vascular endothelial cells. Autophagy. 2021;17:4266–85.
27. Doll S, Proneth B, Tyurina YY, Panzilius E, Kobayashi S, Ingold I, et al. ACSL4 dictates ferroptosis sensitivity by shaping cellular lipid composition. Nat Chem Biol. 2017;13:91–8.
28. Liao P, Wang W, Wang W, Kryczek I, Li X, Bian Y, et al. CD8(+) T cells and fatty acids orchestrate tumor ferroptosis and immunity via ACSL4. Cancer Cell. 2022;40:365–78.e6.
29. Feng H, Schorpp K, Jin J, Yozwiak CE, Hoffstrom BG, Decker AM, et al. Transferrin receptor is a specific ferroptosis marker. Cell Rep. 2020;30:3411–23. e7.
30. Anthonymuthu TS, Kenny EM, Shrivastava I, Tyurina YY, Hier ZE, Ting HC, et al. Empowerment of 15-lipoxygenase catalytic competence in selective oxidation of membrane ETE-PE to ferroptotic death signals, HpETE-PE. J Am Chem Soc. 2018;140:17835–9.
31. Tong J, Li D, Meng H, Sun D, Lan X, Ni M, et al. Targeting a novel inducible GPX4 alternative isoform to alleviate ferroptosis and treat metabolic-associated fatty liver disease. Acta Pharm Sin B. 2022;12:3650–66.
32. Nishiyama K, Takaji K, Kataoka K, Kurihara Y, Yoshimura M, Kato A, et al. Id1 gene transfer confers angiogenic property on fully differentiated endothelial cells and contributes to therapeutic angiogenesis. Circulation. 2005;112:2840–50.
33. Lu L, Zhang RY, Wang XQ, Liu ZH, Shen Y, Ding FH, et al. C1q/TNF-related protein-1: an adipokine marking and promoting atherosclerosis. Eur Heart J. 2016;37:1762–71.
34. Lockman K, Taylor JM, Mack CP. The histone demethylase, Jmjd1a, interacts with the myocardin factors to regulate SMC differentiation marker gene expression. Circ Res. 2007;101:e115–23.
35. Ikawa M, Okazawa H, Tsujikawa T, Matsunaga A, Yamamura O, Mori T, et al. Increased oxidative stress is related to disease severity in the ALS motor cortex: a PET study. Neurology. 2015;84:2033–9.
36. Nie X, Elvington A, Laforest R, Zheng J, Voller TF, Zayed MA, et al. (64)Cu-ATSM positron emission tomography/magnetic resonance imaging of hypoxia in human atherosclerosis. Circ Cardiovasc Imaging. 2020;13:e009791.
37. Southon A, Szostak K, Acevedo KM, Dent KA, Volitakis I, Belaidi AA, et al. Cu(II)(atsm) inhibits ferroptosis: Implications for treatment of neurodegenerative disease. Br J Pharm. 2020;177:656–67.
38. Zilka O, Poon JF, Pratt DA. Radical-trapping antioxidant activity of copper and nickel bis(thiosemicarbazone) complexes underlies their potency as inhibitors of ferroptotic cell death. J Am Chem Soc. 2021;143:19043–57.
39. Rowe D, Mathers S, Noel K, Rosenfeld C. CuATSM phase 2a study confirms disease-modifying effects in patients with sporadic ALS observed in the phase 1 study (1338). Neurology. 2020;94:1338.
40. Li DJ, Evans RG, Yang ZW, Song SW, Wang P, Ma XJ, et al. Dysfunction of the cholinergic anti-inflammatory pathway mediates organ damage in hypertension. Hypertension. 2011;57:298–307.
41. Li DJ, Huang F, Ni M, Fu H, Zhang LS, Shen FM. alpha7 Nicotinic acetylcholine receptor relieves angiotensin II-induced senescence in vascular smooth muscle cells by raising nicotinamide adenine dinucleotide-dependent SIRT1 activity. Arterioscler Thromb Vasc Biol. 2016;36:1566–76.

42. Li DJ, Fu H, Tong J, Li YH, Qu LF, Wang P, et al. Cholinergic anti-inflammatory pathway inhibits neointimal hyperplasia by suppressing inflammation and oxidative stress. Redox Biol. 2018;15:22–33.
43. Tang D, Kang R, Berghe TV, Vandenabeele P, Kroemer G. The molecular machinery of regulated cell death. Cell Res. 2019;29:347–64.
44. Conrad M, Sandin A, Forster H, Seiler A, Frijhoff J, Dagnell M, et al. 12/15-lipoxygenase-derived lipid peroxides control receptor tyrosine kinase signaling through oxidation of protein tyrosine phosphatases. Proc Natl Acad Sci USA. 2010;107:15774–9.
45. Sykes DB, Kfoury YS, Mercier FE, Wawer MJ, Law JM, Haynes MK, et al. Inhibition of dihydroorotate dehydrogenase overcomes differentiation blockade in acute myeloid leukemia. Cell. 2016;167:171–86.e15.
46. Marques RM, Gonzalez-Nunez M, Walker ME, Gomez EA, Colas RA, Montero-Melendez T, et al. Loss of 15-lipoxygenase disrupts Treg differentiation altering their pro-resolving functions. Cell Death Differ. 2021;28:3140–60.
47. Cui W, Liu D, Gu W, Chu B. Peroxisome-driven ether-linked phospholipids biosynthesis is essential for ferroptosis. Cell Death Differ. 2021;28:2536–51.
48. Bao WD, Pang P, Zhou XT, Hu F, Xiong W, Chen K, et al. Loss of ferroportin induces memory impairment by promoting ferroptosis in Alzheimer's disease. Cell Death Differ. 2021;28:1548–62.
49. Wang Y, Yan S, Liu X, Deng F, Wang P, Yang L, et al. PRMT4 promotes ferroptosis to aggravate doxorubicin-induced cardiomyopathy via inhibition of the Nrf2/GPX4 pathway. Cell Death Differ. 2022;29:1982–95.
50. Rong Y, Fan J, Ji C, Wang Z, Ge X, Wang J, et al. USP11 regulates autophagy-dependent ferroptosis after spinal cord ischemia-reperfusion injury by deubiquitinating Beclin 1. Cell Death Differ. 2022;29:1164–75.
51. Liu Y, Gu W. p53 in ferroptosis regulation: the new weapon for the old guardian. Cell Death Differ. 2022;29:895–910.
52. Ide S, Kobayashi Y, Ide K, Strausser SA, Abe K, Herbek S, et al. Ferroptotic stress promotes the accumulation of pro-inflammatory proximal tubular cells in maladaptive renal repair. Elife. 2021;10:e68603.
53. Zhang X, Li LX, Ding H, Torres VE, Yu C, Li X. Ferroptosis promotes cyst growth in autosomal dominant polycystic kidney disease mouse models. J Am Soc Nephrol. 2021;32:2759–76.
54. Zou Y, Henry WS, Ricq EL, Graham ET, Phadnis VV, Maretich P, et al. Plasticity of ether lipids promotes ferroptosis susceptibility and evasion. Nature. 2020;585:603–8.
55. Zhang P, Gao K, Zhang L, Sun H, Zhao X, Liu Y, et al. CRL2-KLHDC3 E3 ubiquitin ligase complex suppresses ferroptosis through promoting p14(ARF) degradation. Cell Death Differ. 2022;29:758–71.
56. Maschalidi S, Mehrotra P, Keceli BN, De Cleene HKL, Lecomte K, Van der Cruyssen R, et al. Targeting SLC7A11 improves efferocytosis by dendritic cells and wound healing in diabetes. Nature. 2022;606:776–84.
57. Chen X, Kang R, Kroemer G, Tang D. Organelle-specific regulation of ferroptosis. Cell Death Differ. 2021;28:2843–56.
58. Cao LL, Riascos-Bernal DF, Chinnasamy P, Dunaway CM, Hou R, Pujato MA, et al. Control of mitochondrial function and cell growth by the atypical cadherin Fat1. Nature. 2016;539:575–8.
59. Ruef J, Rao GN, Li F, Bode C, Patterson C, Bhatnagar A, et al. Induction of rat aortic smooth muscle cell growth by the lipid peroxidation product 4-hydroxy-2-nonenal. Circulation. 1998;97:1071–8.
60. Branchetti E, Poggio P, Sainger R, Shang E, Grau JB, Jackson BM, et al. Oxidative stress modulates vascular smooth muscle cell phenotype via CTGF in thoracic aortic aneurysm. Cardiovasc Res. 2013;100:316–24.
61. Wang L, Yu T, Lee H, O'Brien DK, Sesaki H, Yoon Y. Decreasing mitochondrial fission diminishes vascular smooth muscle cell migration and ameliorates intimal hyperplasia. Cardiovasc Res. 2015;106:272–83.
62. Tang Y, Jia Y, Fan L, Liu H, Zhou Y, Wang M, et al. MFN2 prevents neointimal hyperplasia in vein grafts via destabilizing PFK1. Circ Res. 2022;130:e26–e43.
63. Kuo MTH, Beckman JS, Shaw CA. Neuroprotective effect of CuATSM on neurotoxin-induced motor neuron loss in an ALS mouse model. Neurobiol Dis. 2019;130:104495.
64. Hung LW, Villemagne VL, Cheng L, Sherratt NA, Ayton S, White AR, et al. The hypoxia imaging agent Cull(atsm) is neuroprotective and improves motor and cognitive functions in multiple animal models of Parkinson's disease. J Exp Med. 2012;209:837–54.
65. Chi C, Fu H, Li YH, Zhang GY, Zeng FY, Ji QX, et al. Exerkine fibronectin type-III domain-containing protein 5/irisin-enriched extracellular vesicles delay vascular ageing by increasing SIRT6 stability. Eur Heart J. 2022;43:4579–95.
66. Li DJ, Tong J, Li YH, Meng HB, Ji QX, Zhang GY, et al. Melatonin safeguards against fatty liver by antagonizing TRAFs-mediated ASK1 deubiquitination and stabilization in a beta-arrestin-1 dependent manner. J Pineal Res. 2019;67:e12611.
67. Hua X, Sun DY, Zhang WJ, Fu JT, Tong J, Sun SJ, et al. P7C3-A20 alleviates fatty liver by shaping gut microbiota and inducing FGF21/FGF1, via the AMP-activated protein kinase/CREB regulated transcription coactivator 2 pathway. Br J Pharm. 2021;178:2111–30.
68. Walke GR, Ruthstein S. Does the ATSM-Cu(II) biomarker integrate into the human cellular copper cycle? ACS Omega. 2019;4:12278–85.
69. Shi X, Ohta Y, Nakano Y, Liu X, Tadokoro K, Feng T, et al. Neuroprotective effect of CuATSM in mice stroke model by ameliorating oxidative stress. Neurosci Res. 2021;166:55–61.

AUTHOR CONTRIBUTIONS

PW and DJL conceived and designed research; QXJ, FYZ, JZ, XJW, ZZ, GYZ, JT, DYS and JBZ performed experiments; JZ provided patents samples; QXJ, FYZ, XJW, FMS and PW analyzed data. QXJ, PW and DJL wrote the manuscript. PW, DJL and FMS provided funding. All authors contributed with productive discussions and knowledge to the final version of this manuscript.

FUNDING

This work was supported by the grants from National Natural Science Foundation of China (91849135, 82073915, 81673485, 81773719, 81973312 and 81971306), the National Key Research and Development Project (2018YFA0108301), Shanghai Science and Technology Commission (21XD1424900, 19140904700, 19140904900, 2019CXJQ03 and 21S11901200), Shanghai Shuguang Program (19SG32), Shanghai "Rising Stars of Medical Talent" Youth Development Program-Youth Medical Talents-Clinical Pharmacist Program [SHWRS(2020)_087], and Tongji University-Fundamental Research Funds for the Central Universities (22120210560).

COMPETING INTERESTS

The authors declare no competing interests.

ETHICS APPROVAL

All studies related to human patients were approved by the Ethics Committee of Shanghai Tenth People's Hospital (No. SHSY-IEC-KY-4.0/18-182/01). All animal-related procedures were reviewed and approved by the Institutional Animal Care and Use Committee of Naval Medical University.

ADDITIONAL INFORMATION

Supplementary information The online version contains supplementary material available at https://doi.org/10.1038/s41418-022-01099-5.

Correspondence and requests for materials should be addressed to Dong-Jie Li or Pei Wang.

Reprints and permission information is available at http://www.nature.com/reprints

Publisher's note Springer Nature remains neutral with regard to jurisdictional claims in published maps and institutional affiliations.

Springer Nature or its licensor (e.g. a society or other partner) holds exclusive rights to this article under a publishing agreement with the author(s) or other rightsholder(s); author self-archiving of the accepted manuscript version of this article is solely governed by the terms of such publishing agreement and applicable law.